

Doctoral Thesis (Abridged)

**Bow Shock Instabilities and its Control in front of Concave
shaped Blunt Nose at Hypersonic Mach Number 7**
(マッハ7 極超音速気流中において凹面形状鈍頭物体前方に生じる
離脱衝撃波の不安定性とその制御)

Ashish Vashishtha
アシシュ ヴァシシュタ

Doctoral Thesis

**Bow Shock Instabilities and its Control in front of Concave
shaped Blunt Nose at Hypersonic Mach Number 7**
(マッハ7 極超音速気流中において凹面形状鈍頭物体前方に生じる
離脱衝撃波の不安定性とその制御)

Ashish Vashishtha
アシシュ ヴァシシュタ

Department of Advanced Energy,
Division of Transdisciplinary Sciences,
Graduate School of Frontier Sciences,
The University of Tokyo, Kashiwa

August, 2016

Dedication

This work is dedicated to my wife Shakti Sanago and my daughter Abhavya Vashishtha, my late father, Avdhesh Kumar Sharma, my late grandparents, Mr. Vishambhar Dayal Sharma and Mrs. Reshma Devi, my uncle and aunt Mr. Shashi Bhushan Sharma and Mrs. Ganga Devi Sharma, my beloved brother Mr. Pradhumn Vashishtha, my sister and her husband Mrs. Priya Vashistha Sharma and Mr. Jitendra Sharma.

Abstract

In this study, a concave shaped blunt nose is desired to work as hypersonic decelerator during re-entry mission. Early researches have shown that cavity in front of a blunt body have reduced heating characteristics in supersonic and hypersonic flow. During the wind tunnel test, it was also found in early researches that cavity in front of blunt body have violent bow shock fluctuations associated with it. The physics of these violent large amplitude bow shock fluctuations is not completely understood. Moreover, to utilize the concave shape blunt nose as hypersonic decelerator, it is necessary the bow shock in front of concave shape geometry should be stable, otherwise large amplitude oscillatory or uncontrolled bow shock may have dynamic and variable heating effects on the re-entry vehicle.

As a first step, the experiments are conducted at hypersonic Mach number 7 for concave shape hemispherical shell along with flat plate and convex shape blunt nose to have a comparative analysis of these three basic geometries. During the experiments, the force measurement and time-resolved flow visualization is performed by using high-speed camera with Schlieren system at 50000 frames per second. Further to characterize the bow shock fluctuations from the time-resolved high-speed video, an image processing method has been established to get the bow shock fluctuation data as a time series. From the analysis of time series of bow shock fluctuations, it is found that the bow shock in front of concave shaped blunt nose behaves like a nonlinear oscillator similar to duffing oscillator, which has nonlinear restoring force. Hence, the analogies are drawn from the duffing oscillator to understand the flow phenomenon involved in large amplitude bow shock fluctuations. Further, from the captured high-speed image frames, proper orthogonal decomposition have been performed, which gives information regarding two kind of orthogonal modes in large amplitude bow shock fluctuations as back and forth flow motion and flow moving from the sides of concave cavity for first few modes. The effect of change in angle of attack in front of concave shaped blunt nose is also studied and it is found that for angle of attack greater than 7° , the bow shock remains steady as the bow shock becomes slightly away from one edge and closer to the other edge, which gives opening for disturbance to move from cavity from one direction.

Based on above understanding of large amplitude bow shock fluctuations in front of concave shaped blunt nose, two kind of passive control methods are employed to the concave shaped blunt nose to achieve dual objectives. One objective is to understand the mechanism of bow shock instability

by analyzing the effects of different passive controls and second objective is to have the best flow control mechanism to stop the large amplitude bow shock fluctuations. One kind of passive control methods are based on the flow control around the edge of concave cavity as flat base, notch and tab controls. The second kind the passive controls are based on the back and forth flow in the cavity as breathing control, spike control and crosswire control. The experiments are performed in hypersonic wind tunnel at Mach 7 for the study of passive control methods. And the effectiveness of control methods are analyzed by force measurement and bow shock displacement analysis, which is obtained by using the high-speed time-resolved Schlieren video. By the studies of flow control, it is found that the cavity based control methods spike and crosswire works better than other control mechanism studied. However, other passive controls methods are also partial effective but their effect is not as promising as crosswire and spike. This gives the further understanding that concave shape of blunt nose offers larger area for growth of vortices in the cavity as compare to flat or convex shape, which may introduce the nonlinear effects in high pressure gradient after the bow shock, for bow shock in front of concave cavity fluctuation system. And, the vortex manipulation offered by cavity based controls, spike and crosswire, work best among the other control methods.

Further, to access the three dimensional flow field inside the concave cavity, three dimensional numerical simulations, in front of concave hemispherical shell along with flat and convex blunt nose are performed by solving unsteady compressible Navier-Stokes equations for wind tunnel test conditions. However, the numerical simulations for concave shape geometry are not stable and breaks down as the large shock displacement starts (system becomes nonlinear). But, the onset of large amplitude bow shock motion have been captured for concave shaped blunt nose and further flow physics for large shock displacement have been explained from all the experimental and numerical results. It is found that deformation in ring vortex inside the cavity leads to large vortical motion from side of concave shaped blunt nose, which results in large amplitude bow shock fluctuations.

Acknowledgments

I would like to express my deepest gratitude to my advisor, Professor Kojiro Suzuki for providing me the opportunity to study under his valuable guidance. I would like to sincerely thank him for all the encouragement and support provided by him towards my research from the day, I joined here. His patience and affability helped me to not only increase my inquisitive approach towards my research but to gain further deeper understanding of the subject.

I would like to sincerely express my thankfulness to Professor Ethirajan Rathakrishnan, Department of Aerospace Engineering, Indian Institute of Technology, Kanpur, INDIA, for his suggestion to apply at Suzuki Lab for my higher studies. I would like to owe a special thanks to him for being my advisor during my masters research, which has become the basis for my deeper understanding of gas dynamics.

I am highly obligated to Assistant Professor, Yasumasa Wanatabe, for giving me guidance through fruitful discussions and your countless supports from learning of numerical methods, using rapid prototyping machine, and to provide help during experiments at wind Tunnel facility.

I would like to take this opportunity to thank all my lab mates at Suzuki lab working together and discussing on numerous ideas. I would like to thank Dr. Rey Yamashita, Dr. Y. Ohmichi, Dr. H. Shibata, Mr. Kawauchi Daichi, Mr. Mohammad Samara for always be there for discussion and helping out each other.

I would like to thank my family back in India, my uncle and aunt, my brother and sister, for their support and encouragements at all the stages. I would like to pay my great regards to my late grandmother, who was my first teacher and source of my inquisitive thinking and pursuit for knowledge. I would like to pay my deep regards to my late father for being the source of inspiration for me, which has helped me to be calm and stable at all the time.

My heartfelt love and gratitude to my wife, Shakti for her co-operation, endurance and patience during the crucial phase of my research program. She has come so beautifully into my life, adding the love and care, I so much needed, and backing me up with her incessant support.

I would like to acknowledge the support at Kashiwa Hypersonic Wind Tunnel Facility and Supercomputing Division, Information Technology Center, The University of Tokyo. I would also like to acknowledge Ministry of Education, Culture, Sports, Science and Technology (MEXT), Govt. of Japan for providing financial support for my doctoral research at The University of Tokyo.

Contents

Abstract	ii
Acknowledgments	iv
Contents	v
List of Figures	ix
List of Tables	xiv
1 Introduction	1
1.1 Overview	1
1.1.1 Atmospheric Entry	1
1.1.2 Characteristics of Hypersonic Flow	3
1.1.3 Bow Shock Instability	5
1.2 Previous Studies: Frontal Cavity in High-speed Flows	7
1.3 Flow control Methods	11
1.3.1 Active Control	11
1.3.2 Passive Control	11
1.4 Need for study of Bow-Shock Instability and Control	13
1.5 Objectives	17
1.6 Outline of Thesis	18
Experimental Study	21
2 Experimental Methodology	22
2.1 Hypersonic Wind Tunnel Facility	22
2.1.1 Wind Tunnel Specifications	22

2.1.2	Instrumentation for Force Measurement	24
2.1.3	Optical System for Flow Visualization	25
2.2	Experimental Models	26
2.2.1	Basic Geometries	26
2.2.2	Passive Flow Control Geometries	28
2.3	Experimental Procedure	30
2.3.1	Operating Conditions	30
2.3.2	Force Measurement	33
2.3.3	Flow Visualization	33
2.4	Data Reduction	34
2.4.1	Force Coefficients	34
2.4.2	Shock Displacement Measurement	37
2.4.3	Image Time Matrix Formulation	40
2.5	Estimation of Free stream disturbances	42
2.6	Data Accuracy	44
3	Experimental Results for Basic Geometries	46
3.1	Outline	46
3.2	Force analysis for basic geometries	47
3.3	Bow shock displacement analysis for basic geometries	50
3.3.1	Region of Visibility	50
3.3.2	Bow Shock Displacement Time History	53
3.3.3	Nonlinear behavior of Bow Shock	57
3.4	Bow shock instability patterns for basic geometries	64
3.5	POD modes for concave shape geometry	72
3.6	Effect of Angle of Attack for Concave Shape	75
3.6.1	Force analysis	75
3.6.2	Bow shock displacement analysis	78
3.7	Conclusion	84
4	Experimental Results for Passive Flow Controls	86
4.1	Outline	86
4.2	Edge based Passive Flow Controls	87
4.2.1	Force Analysis	88

4.2.2	Bow Shock Displacement Analysis	90
4.3	Cavity based Passive Flow Controls	98
4.3.1	Force Analysis	99
4.3.2	Bow Shock Displacement Analysis	101
4.4	POD modes for spike and crosswire controls	109
4.5	Understanding of instability mechanism by control study	114
	Numerical Study	116
5	Numerical Methodology	117
5.1	Governing Equations	117
5.1.1	Unsteady Compressible Navier Stokes Equations	117
5.1.2	Nondimensionalization	119
5.1.3	Generalized Governing Equations	120
5.2	Numerical Techniques	122
5.2.1	Evaluation of Inviscid Fluxes	122
5.2.2	Evaluation of Viscous Fluxes	125
5.2.3	Time Integration	126
5.3	Problem Setting	126
5.3.1	Computational Domain	126
5.3.2	Initial and Boundary Conditions	128
5.3.3	Data Extraction	129
6	Numerical Results	131
6.1	Numerical Results for Flat and Convex Geometry	131
6.2	Numerical Results for Concave Geometry	134
6.3	Numerical and Experimental Bow Shock Deformation	139
6.4	Development of bow shock deformation in numerical study	141
7	Discussion on Bow shock Instability Mechanism	146
7.1	Findings from Experimental and Numerical Studies	146
7.2	Mechanism of bow shock behavior around concave shape	148
7.2.1	Stable Linear bow shock fluctuations	149
7.2.2	Transition to nonlinear fluctuations	150
7.2.3	Bow shock stabilizing mechanism for angle of attack	153

7.3	Flow physics of passive control methods	154
7.4	Applicability of the study in other flow regimes	156
8	Conclusions	159
	References	161
	Appendices	167
A	Proper Orthogonal Decomposition : Method of Snapshots	168

List of Figures

1.1	Different flow regimes during atmospheric entry	2
1.2	Typical hypersonic flow field around different curvature blunt noses	6
1.3a	Various passive flow control for upstream flow	12
1.3b	Various passive flow control for jets	12
1.4	Disturbance in bow shock in front of conventional convex blunt nose	14
1.5	Schematic of Passive flow control methods devised in this study to concave shaped blunt nose	16
1.6a	Road Map of the study	19
1.6b	Road Map of the study (continued)	20
2.1	Pictorial view of hypersonic wind tunnel facility and test-section	23
2.2	Force measurement instrumentation (a) Force Balance, (b) Data Logger, (c) Signal Conditioner	24
2.3	Schematic representation of twin mirror Schlieren system	25
2.4	Pictorial view of (a) Light Source (b) High speed camera with lens	25
2.5	Geometric details for (a) Flat Plate, (b) Convex Shape and (c) Concave Shape basic geometries	27
2.6	Pictorial View for Concave Hemispherical Shell (a) with connecting rod (b) attached in the test-section	27
2.7	Geometric details for Edge based passive flow control (a) Flat Base, (b) With Notch (c) with Tab	28
2.8	Pictorial View of edge based passive flow controls (a) Flat Base, (b) With Notch (c) with Tab	29
2.9	Geometric details for cavity based passive flow controls (a) With Breathing Holes, (b) With Spike (c) with Crosswire	29
2.10	Pictorial view of cavity based passive flow controls (a) With Breathing Holes, (b) With Spike (c) with Crosswire	30
2.11	Stagnation pressure variation during wind tunnel operations for zero AOA experiments	31

2.12	Stagnation temperature variation during wind tunnel operations with drag force data for zero AOA experiments	31
2.13	Stagnation pressure variation during wind tunnel operations for variation of angle of attack	32
2.14	Stagnation temperature variation during wind tunnel operations with AOA data for angle of attack	33
2.15	Force balance calibration for normal and axial force	35
2.16	Force balance calibration for side force and pitching moment	35
2.17	Force balance calibration for yawing and rolling moment	36
2.18	Steps from (a) to (f) for image processing method used to detect the bow shock edges	38
2.19	Shock displacements measured for locations A, B and C for (a) concave (b) flat (c) convex shaped blunt noses	39
2.20	Steps from (a) to (e) for image processing method used to convert image into image vector	41
2.21	Formation of image time matrix for fluctuations	41
2.22	(a) Side View, (b) Top View of pressure tubes, (c) Schlieren Image and PSD plots for fluctuations measured at (d) 10 kHz, (e) 100 kHz	43
3.1	Time history for (a) Drag, (b) Lift (c) Side force coefficients and (d) Loci of lift vs side force coefficients for flat, convex and concave shaped blunt nose	48
3.2	Schlieren images of stable bow-shock for (a) convex, (b) flat and (c) concave shaped blunt nose	49
3.3	Schematic of three dimensional bow shock and its two dimensional Schlieren projection for (a) convex and (b) flat blunt noses	50
3.4	Schematic of three dimensional bow shock and its two dimensional Schlieren projection for different bow shock deformation in front of concave blunt nose	52
3.5	Different 2-D Schlieren patterns of bow shock observed in front of concave blunt nose and corresponding schematic of three dimensional bow shock (i) no deformation and deformation in (ii)a Region I, (ii)b Region III, (iii) Region II, (iv) Region IV	53
3.6	Time history of bow shock displacement for convex shaped blunt nose	54
3.7	Time history of bow shock displacement for flat plate	54
3.8	Time history of bow shock displacement for concave shaped blunt nose	55
3.9	(a) Probability density and (b) Cumulative distribution function of bow shock displacements for convex shape	58
3.10	(a) Probability density and (b) Cumulative distribution function of bow shock displacements for flat shape	58
3.11	(a) Probability density and (b) Cumulative distribution function of bow shock displacements for for concave shape	59
3.12	(a) Double well potential curve for one case of duffing equation (b) Proposed potential curve for bow shock displacements along centerline in front of concave shape	60

3.13	Power Spectrum for shock displacement along upper edge center (δ_A)	63
3.14	Bow shock disturbance pattern in front of convex shape blunt nose	65
3.15	Bow shock disturbance pattern in front of flat plate blunt nose	66
3.16	Bow shock displacement for one instability pattern	68
3.17	Initiation of bow shock instability in front of concave shaped blunt nose	69
3.18	Bow shock instability pattern in front of concave shaped blunt nose	70
3.19	Normalized POD Eigenvalues of first 20 modes for concave shape blunt nose	72
3.20	Time averaged Image data (mean) for time interval 0 to 0.4 s	73
3.21	First six spatial POD modes captured for time interval 0 to 0.4 s	73
3.22	Time averaged (a) Drag, (b) Lift (c) Side Force Coefficients with error bars represent standard deviation (σ) for concave shaped blunt nose with change in angle of attack .	76
3.23	Lift vs Side Force Coefficient plots for 3 second time (a) Positive (b) Negative (c) 6° to 9° angle of attacks	77
3.24	Instantaneous Steady Schlieren image for bow shock in front of concave shape at all angle of attacks	78
3.25	Bow shock displacement along centerline (δ_B) for positive angle of attacks	79
3.26	(a) Probability density (b) Cumulative distribution plot for (δ_B) at positive angle of attacks	80
3.27	Bow shock displacement along centerline (δ_B) for negative angle of attacks	81
3.28	(a) Probability density (b) Cumulative distribution plot for (δ_B) at negative angle of attacks	82
3.29	Bow shock displacement along centerline (δ_B) for (δ_B) at 6° to 9° angle of attacks . .	83
3.30	(a) Probability density (b) Cumulative distribution plot for 6° to 9° angle of attack .	84
4.1	(a) Drag Coefficient for edge based control compared with no control and Lift and side force locus for (b) flat base, (c) notch and (d) tab controls	88
4.2	Instantaneous Schlieren images of stable bow-shock for edge based controls	89
4.3	Time history of Bow shock displacement for concave blunt nose with flat base control	91
4.4	Comparison of PDF and CDF for concave blunt nose with flat base control and without control	92
4.5	Time history of Bow shock displacement for concave blunt nose with notch control . .	93
4.6	Comparison of PDF and CDF for concave blunt nose with notch control and without control	94
4.7	Time history of Bow shock displacement for concave blunt nose with tab control . . .	95
4.8	Comparison of PDF and CDF for concave blunt nose with tab control and without control	96
4.9	Power Spectrum for shock displacements along centerline (δ_B) for edge based controls	98

4.10	(a) Drag Coefficient for edge based control compared with no control and Lift and side force locus for (b) breathing, (c) spike and (d) crosswire controls	100
4.11	Instantaneous Schlieren images of stable bow-shock for edge based controls	101
4.12	Time history of Bow shock displacement for concave blunt nose with breathing control	102
4.13	Comparison of PDF and CDF for concave blunt nose with breathing control and without control	103
4.14	Time history of Bow shock displacement for concave blunt nose with spike control	104
4.15	Comparison of PDF and CDF for concave blunt nose with spike control and without control	105
4.16	Time history of Bow shock displacement for concave blunt nose with crosswire control	106
4.17	Comparison of PDF and CDF for concave blunt nose with crosswire control and without control	107
4.18	Power Spectrum for shock displacement along centerline (δ_B) for cavity based controls	108
4.19	Normalized POD Eigenvalues of first 20 modes for (a) Spike Control (b) Crosswire Control (c) Comparison with no control	109
4.20	Time averaged Image data (mean) for time interval 0 to 0.4 s for (a) Spike Control (b) Crosswire Control	111
4.21	First six spatial POD modes captured for Spike Control during time interval 0 to 0.4 s	111
4.22	First six spatial POD modes captured for Crosswire Control during time interval 0 to 0.4 s	112
4.23	First six spatial POD modes captured for Crosswire Control during time interval 0.8 to 1.2 s	112
5.1	Elliptic grid for flat and convex geometries shown as section of three dimensional grid with zoomed view	127
5.2	(a) Elliptic grid section for concave geometry and (b) three dimensional view of domain	127
5.3	Flow properties calculated along stagnation line and along edge center as shown above	130
6.1	Numerical drag coefficient for flat and convex shaped blunt nose	132
6.2	Comparison of density gradient magnitude contour in front of flat and convex shaped blunt nose with experimental Schlieren image	132
6.3	Time history of nondimensional pressure ($P/\rho U_\infty^2$) along the stagnation line	133
6.4	Time history of nondimensional pressure ($P/\rho U_\infty^2$) along the circumference of circle near the forward edge	134
6.5	Time history of drag coefficient for concave geometry compared for three different grids	135
6.6	Lift vs side force coefficients for concave 151x151x151	136
6.7	Power spectrum plot for pressure at the center of cavity time series	136
6.8	Time history of nondimensional pressure ($P/\rho U_\infty^2$) along the stagnation line	138

6.9	Time history of nondimensional pressure ($P/\rho U_\infty^2$) along the circumference of circle near the forward edge	139
6.10	Three dimensional vortex structure as seen by Q-criterion ⁶⁴ and density gradient magnitude for shock (left), X-Y plane streamlines with density gradient magnitude (middle), similar experimental Schlieren image (right)	140
6.11	Pressure Coefficient for center of the cavity and edge center along Y- and Z- direction	142
6.12	Three dimensional vortex structures as seen by Q-criterion and density gradient magnitude for shock (left), X-Y plane streamlines with density gradient magnitude (right)	143
7.1	Schematic for linear bow shock behavior in front of concave blunt nose	149
7.2	Schematic for Large deformation mechanism of bow shock	151
7.3	Schematic for Large deformation mechanism of bow shock	153
7.4	Schematic for effectiveness of edge based passive control methods	154
7.5	Schematic for effectiveness of cavity based passive control methods	155

List of Tables

2.1	Hypersonic Wind Tunnel Specification ⁴⁶	22
2.2	Balance Calibration Matrix for data conversion	37
3.1	Time-averaged force coefficients with standard deviation (σ) for 5 to 15 seconds	48
3.2	Fraction of Energy Captured by each POD mode for different time intervals	74
4.1	Time-averaged force coefficients for edge based flow controls with standard deviation (σ) for 5 to 15 seconds	89
4.2	Time-averaged force coefficients for cavity based flow controls with standard deviation (σ) for 5 to 15 seconds	101
4.3	Fraction of Energy Captured by each POD mode for different time intervals	109
4.4	Performance of Passive Control Methods	115
5.1	Flow conditions for numerical simulation	128
6.1	Drag and Shock stand off distance comparison for numerical and experimental results	133
6.2	Time-averaged drag coefficient and shock stand off distance for different grid configuration of concave blunt nose, when bow shock behaves linearly	135

Chapter 1

Introduction

1.1 Overview

1.1.1 Atmospheric Entry

Bringing spacecrafts from the outer space to surface of earth or other planet is one of the challenging task in space transportation. There are three main requirements during this phase of space mission: sufficient deceleration to bring the spacecrafts from higher orbital velocities to rest, tackle the high temperature generated because of traveling into denser atmosphere, and landing safely. During entry, descent and landing to earth or any other planet, the spacecrafts travel through different flow regimes. The kind of flow field around the spacecraft determine it's aerodynamic performance, because the forces and moments experienced by the body are different in different flow field.

The flow field can be classified in different regimes, depending on changes in fluid properties. It can be classified as incompressible and compressible flow field, depending on density variation as negligible small (less than 5 %) and considerable (greater than 5 %), respectively¹. Furthermore, it can be classified as low-speed (temperature changes less than 5 %) and high-speed (temperature changes more than 5 %). The Mach number M , which is defined as ratio of local flow velocity to local speed of sound,² limit for incompressible and compressible flow field is 0.3. Similarly, for low-speed and high-speed flow field, the Mach number limit is 0.5. Based on Mach number M , the flow field can divided into four regimes. When Mach number is less than 0.8 ($M < 0.8$), the flow field is called subsonic; when $M \approx 1$ ($0.8 \leq M \leq 1.2$), the flow field is termed as transonic flow, Mach number from 1.2 to 5 is called supersonic regime, and for Mach number greater than 5 ($M > 5$) is referred to hypersonic flow field². When an arbitrary body moves in a fluid, it experiences forces and

moments due to relative fluid flow that is taking place around it. The force on the body along the flow direction, retarding the body motion is called drag force³. The force acting perpendicular to flow direction to counter the weight of the body is called lift force and in three-dimensional flow-field, force acting perpendicular to lift and drag force in lateral direction is called side force. These forces can be non-dimensionalized by dynamic pressure and maximum cross-sectional area of body and converted to static force coefficients as drag coefficient, lift coefficient and side force coefficient. The overall drag force depends on shape and size of the body and is important parameter for design of transport vehicle as shapes experiencing minimum drag require lesser power to propel, while higher drag is desired to retard the motion of flying vehicle.

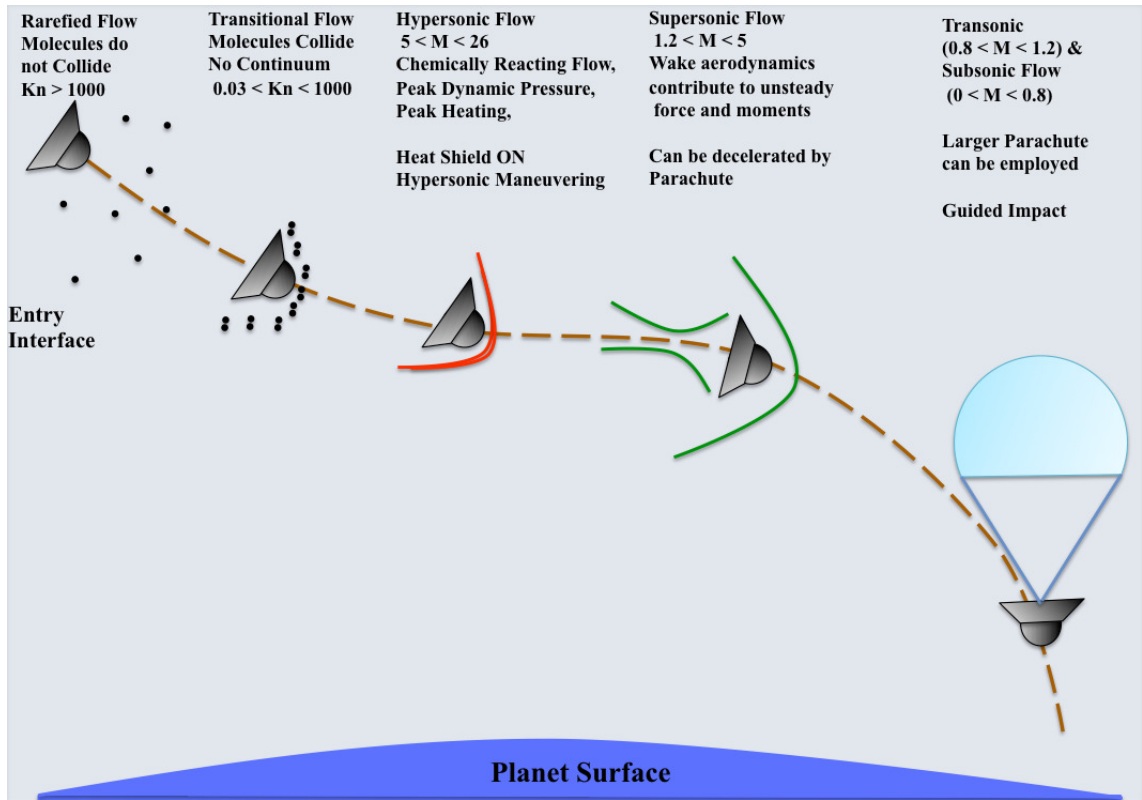


Figure 1.1: Different flow regimes during atmospheric entry

The movement of spacecrafts through different flow regimes during atmospheric entry flight is shown in schematic diagram in Fig. 1.1. The entry in the atmosphere starts with low-density free molecular flow regime, where molecules does not collide to each other. The speed during entry of atmosphere can be as high as 12 km/s in case of earth. As the altitude decreases, the vehicle reached to transitional flow regime. Further with decrease in altitude and increase in density, the vehicle reaches hypersonic flow regime of peak heating and peak dynamic pressure. In this flow regime, heat shield is required to avoid the peak heating to reach the surface of the body. Further, as vehicle

speed reduces, it reaches the supersonic flight region, where wake aerodynamics plays important role in dynamic stability of the vehicle. In transonic and subsonic speeds, the flight path can be precisely controlled and larger parachute can be deployed to further stop the vehicle at the ground.

Two kind of maneuvers can be designed for atmospheric entry as ballistic entry or lifting entry. During entry motion, when the drag force is always acting opposed to the line of flight, it is defined as ballistic entry. In lifting entry, lift force is generated along with drag force throughout the motion and flight path can be adjusted while the vehicle is slowing down. The important parameters for designing and control of ballistic entry is ballistic coefficient (β) which is defined as ratio of mass and total drag force acting on the maximum cross sectional area of vehicle ($\beta = m/C_D A$). To have quick time in deceleration and lower peak temperature, it is required to have lower ballistic coefficient for atmospheric entry, which means higher drag for the moving vehicle or bigger cross sectional area, hence the blunt nose shapes are best suited for ballistic entry. For lifting entry, the important parameter to design such a flight is lift to drag ratio. It is required to have streamlined body to have adequate lift to drag ratio. The peak temperatures for lifting re-entry can be well below the peak temperature of ballistic entry, but the duration of flight can be longer. During lifting entry, although lower peak temperature, but continuous heat load acting on the flight vehicle for longer time, requires vehicle structure to sustain the same. Hence, the hypersonic flow field regime of atmospheric entry is one of the crucial phase because, the spacecraft is exposed to high dynamic loads and high temperature.

1.1.2 Characteristics of Hypersonic Flow

In subsonic flow field, any perturbation can propagate with speed of sound, which is higher than the flow speed, but in supersonic and hypersonic flow regimes the perturbations travel slower than the flow speed. This results in formation of compression and expansion waves in supersonic and hypersonic flow field. The total energy content of flow field is called total enthalpy, it is sum of static enthalpy and kinetic energy. In a subsonic flow, most of the total enthalpy is invested in static enthalpy and changes in Mach number are largely due to changes in flow velocity. In transonic flow both static enthalpy and kinetic energy are comparable, and the Mach number changes rapidly because both the speed of sound and flow velocity are changing. In supersonic flow field, the investment of total enthalpy is more in kinetic energy than in static enthalpy. But in hypersonic flows, the bulk to total temperature is invested in kinetic energy and the changes in Mach number is largely because the static temperature, hence due to local speed of sound. In supersonic and hypersonic flow field, the total drag force on a moving body consists of three main components as wave drag (due to formation of strong compression front at the nose of body called shock waves), base drag (due to creation of suction region at the base because of flow separation) and skin friction drag (due to friction between body surface and fluid).

Further, supersonic and hypersonic flows are essentially wave dominated flows. Any change in flow properties are caused by these waves. The compression in flow field is caused by shock waves and expansion is caused by number of expansion waves. The shock may be defined as a compression front across which the flow properties change abruptly. The shock waves are classified as normal shock, oblique shock and detached bow shock. Normal shock is defined as compression wave front normal to the flow direction across which flow properties change abruptly, whereas oblique shocks are compression front at an angle to the flow direction across which flow properties and flow direction abruptly change². Bow shock is a detached compression front, which is combination of normal shock and infinite oblique shocks, forms in front of blunt nose. Shock strength is defined as percentage of pressure increase across the shock. Normal shock is the strongest shock wave. At a Mach number, a maximum turning angle for the flow field exists, below which the shock wave is attached to the body, and oblique in nature. After a weak oblique shock, the flow may remain supersonic. For more than maximum flow turning, the shock becomes detached and there is formation of bow-shock. Qualitatively, supersonic and hypersonic flows seems similar, however hypersonic flows are essentially physically different from supersonic flow. The main characteristics of hypersonic flows are as follows^{4,5}:

- Thin shock-layer: In supersonic and hypersonic flows, the flow field between the shock wave and the body is defined as shock layer. For hypersonic flow, the shock wave becomes stronger and closer to the body, hence it can be classified as thin shock layer.
- Vorticity Interaction: The stronger shock wave in hypersonic flows ahead of the body increases the entropy of the flow significantly after the shock. In case of bow shock, the entropy near the central region of bow-shock (approximately normal shock) increases maximum as compare to flow passing through the oblique shock region of bow shock. Hence, it generates the entropy gradient in lateral direction. The region of lateral entropy gradient along the surface of body is called entropy layer. In this entropy layer, flow can become highly rotational as suggested from Crocco's theorem for compressible flow². The interaction of high vorticity region of entropy layer with boundary layer is called vorticity interaction.
- Viscous Interaction: The boundary layer thickness grows more rapidly at hypersonic flows because the higher kinetic energy of flow field, which is dissipated within the boundary layer, leads to rise in temperature and reduction in density in the boundary layer. The thick boundary layer can significantly interact with the inviscid flow outside the boundary layer, and this is called viscous interaction. Viscous interaction can also increase the skin friction as well as the heat transfer near the nose.
- High Temperature flow: The dissipation of high kinetic energy of hypersonic flow can increase the temperature in boundary layer too high, that may excite the vibrational internal energy

of molecules, which may lead to dissociation and ionization in the gas. Apart from boundary layer, the nose region of blunt body can exhibit the high temperature effects as the region of normal shock wave, which is responsible for higher temperature near nose region. This may lead to chemically reacting very hot flow in shock layer in nose region and boundary layer. The high temperature in boundary layer region and nose region can induce higher heat transfer to the body surface called as aerodynamic heating. The aerodynamic heating includes the convective heating because of temperature gradient at body surface and radiative heating because of high temperature of the gas itself in shock layer.

- Low density flow: During atmospheric entry of space vehicle, it flies at the outer layer of atmosphere, which has very low density. Because of very low density, the distance between air molecules can be as high as the characteristic length of the vehicle itself. This leads to break down in continuum medium approach of flow study, hence the flow field must be studied by concepts of kinetic theory of gases. The important parameter that governs low-density flow regime is called Knudsen number, defined as ratio of free molecular distance and characteristic length of vehicle ($Kn = \lambda/L$). When Knudsen number is very small ($Kn < 0.03$), the flow field can be analyzed by continuum concepts, while very high Knudsen number ($Kn > 1$) flows should be treated as free molecular flow. For $0.03 < Kn < 1.0$, the flow regime is called transitional flow regime.

However, based on Mach number hypersonic flow regime has been defined for $M > 5$, but there is no such strict limit, when flow-field exhibit the above mentioned flow physics. Hence, hypersonic flows can be best defined as flow regime, where some or all the above physical phenomenon become progressively more important as the Mach number increases to higher value.

1.1.3 Bow Shock Instability

In supersonic and hypersonic flows, bow shock formation occurs in front of blunt nose, or conical nose, when the flow turning angle is more than the critical angle for particular Mach number. In general, the bow shock formed in front of convex spherical nose can be visualized as steady and stable in experiments by using normal camera (25 ~ 30 fps) with optical visualization methods³. However, high frequency oscillation in bow shock can be visualized with high-speed camera for decreased radius of curvature geometry, in other words for blunt nose shapes with higher bluntness. But in case of concave shaped blunt nose (negative radius of curvature), large amplitude violent fluctuations in bow shock have been visualized even with normal camera. The schematic of typical hypersonic flow field around different curvature geometries have been shown in Fig. 1.2.

In case of convex blunt nose shape in Fig. 1.2a, a steady detached bow shock formed ahead of

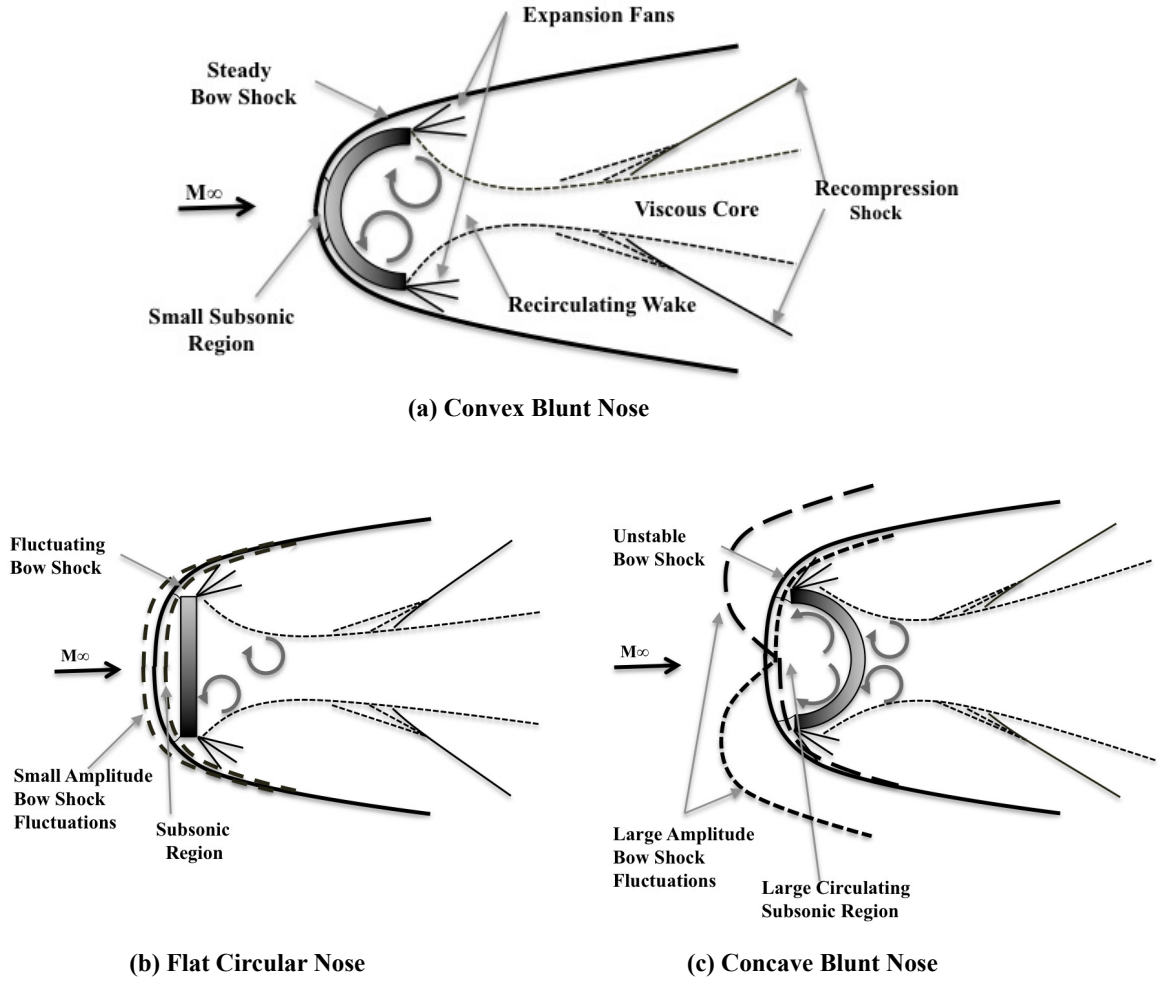


Figure 1.2: Typical hypersonic flow field around different curvature blunt noses

the nose closer to the body surface. The bow shock has maximum strength near the center region as flow has maximum turning near the center, which leads to subsonic zone after the bow shock near center region. However, moving along the surface of convex shaped blunt nose, the flow turning reduces as well as shock strength reduces and flow can have higher supersonic speeds behind the bow shock, which will be maximum near the edge of the surface. After the edge of the surface, flow encounters larger area to expand, which leads to formation of expansion fans near the edge and flow separation. Expansion fans increase the flow speed further, this leads to low pressure region at the base, which can contribute to the base drag of blunt nose shape. The wake region near the base can be very complex and dominated by recirculating zones. As the pressure in the near wake region is low, free shear layer after the flow separation as well as the streamlines from the outer inviscid flow can merge together in a narrow zone around the wake axis forms neck region. The flow which is directed towards the neck region after the flow separation further, needs to turn back towards the wake axis, hence a re-compression shock forms near the neck region. After the neck region, the wake thickness increases suddenly and viscosity effects are dominant in this region, which is called viscous core region.

Fig. 1.2b and c are drawn as schematic of hypersonic flow field around the flat circular blunt nose and concave hemispherical blunt nose according to above discussion. As the bluntness of the nose increases, the region of strong bow-shock becomes bigger near the center of the body, which leads to bigger subsonic region in the front of the body. However increase in the bluntness also leads to bigger recirculation region at the base and far lesser base pressure, hence the overall drag coefficient increases as bluntness of the nose increases. As the subsonic zone increases in front of flat circular blunt nose as shown in Fig. 1.2b, the bow shock exhibits small amplitude, high frequency fluctuation, which can be visualized by high-speed camera⁶. For concave shaped hemispherical blunt nose (Fig. 1.2c), the subsonic zone can become further bigger and extend inside the cavity, where recirculation zone can be formed. The bow shock shows large amplitude violent shock fluctuations in front of concave shaped blunt nose as shown in Fig. 1.2c with two different dotted lines. These violent fluctuations can be visualized by optical visualization methods using normal camera. Although the bow shock is unstable in front of concave shaped blunt nose, the time averaged overall drag coefficient can be higher than convex shape geometry. The mechanism of these violent bow shock fluctuations in front of cavity at high-speed flows is not completely understood. The main motivation for current study is to utilize high drag configuration of concave shaped blunt nose as hypersonic decelerator in atmospheric entry flight regime. However, the unstable bow shock can influence the forces acting on the body as well as heat transfer, hence, it is required to understand the mechanism of shock fluctuations in front of concave shaped blunt nose and provide flow control method to stabilize the bow shock in front of concave shaped blunt nose. In the next section, literature survey have been performed for different studies on frontal cavities in high-speed flows and key findings are discussed.

1.2 Previous Studies: Frontal Cavity in High-speed Flows

The early researches for concave shape cavity in the blunt nose were mainly focused on heat transfer measurements and proving that the cavity in front of blunt nose provides reduced heating in comparison of convex shape blunt nose at supersonic and hypersonic Mach numbers. Hopko et al.⁷ had obtained experimental data for heat transfer to the stagnation point for convex and concave hemispherical nose shapes and hemispherical depression on a 30° blunt nose cone for Mach number up to 8.5. He observed that heating at the stagnation point of concave shape hemispherical nose is $1/3^{rd}$ at Mach number 2 and approximately $1/10^{th}$ at Mach Number 8 as compare to convex shape hemispherical nose. Cooper et al.⁸ had studied concave hemispherical nose experimentally and observed that flow field alternates in random manner between steady and unsteady flow for angle of attack of the order of 2° or less, with low heat transfer associated to steady flow and high heat transfer associated to unsteady motion of bow shock. For higher angle of attacks, the steady bow shock and low heat

transfer was observed except for Mach 4.5 and angle of attack 15° , when shock becomes unsteady. The heat transfer coefficients for unsteady configuration were 6 to 7 times higher than the coefficients for steady flow. For steady flow, heat transfer coefficients at stagnation point of concave blunt nose varied from 20 to 50 % of convex shape hemisphere. Markley⁹ have measured heat transfer coefficient and pressure for 5-inch diameter hemispherical concave cavity in the cylindrical nose at Mach 2.0 in free jet. It was observed that up to 60° on the concave region, the surface pressure was equal to total pressure behind the shock at angle of attack of $0, \pm 5^\circ, \pm 10^\circ$. The heat transfer coefficient at stagnation point is 40 % of that on the same size of convex hemisphere at zero angle of attack and there is no increase at angle of attack $\pm 5^\circ, \pm 10^\circ$. The highest local heat transfer coefficient was measured immediately inside the lip at all angle of attack with same magnitude. Detailed investigation of heat transfer to concave hemispherical nose on a cylindrical body had been done by Levine et al.¹⁰ under free flight conditions at Mach number 3.5 to 6.6. It was observed that heat transfer coefficient at the stagnation point varied from 0.05 to 0.13 times the theoretical convex hemispherical values at Mach 4 to 6.6. At Mach 5, the total heat input, which is integrated over the surface of concave cavity, was 0.55 and 0.76 times of the theoretical value for convex shape and flat shape nose, respectively. Very high heating rates associated with unsteady flow field observed by Cooper et al.⁸ in wind tunnel test-section were not observed in free flight test by Levine et al.¹⁰. Johnson¹¹ had qualitatively investigated blunt bodies with cylindrical, conical and hemispherical surface cavities in helium hypersonic flow at Mach number 21.6 and suggested that continuous formation and shedding of vortices in the cavity may lead to deeper pits during atmospheric passage of observed meteorites. The bow shock in front of cylindrical and conical surface cavities blunt nose at 7000 frames per second was observed steady, while small injection of helium or air jet into stagnation zone leads to violent bow-shock oscillations. He further observed that bow shock in front of hemispherical cavity on flat face of cylinder or on hemisphere exhibit non-oscillatory shock layer instability even without injection of air or helium jet. Baryshnikov et.al¹² have also studied instability of bow shock in front of segmental body in dissociating gas environment of CF_2Cl_2 and classified the instabilities as small deformation, large deformation and complete destruction of bow shock. He aimed to reduce the drag by destabilizing and destructing the bow shock. He further relates the bow shock instabilities with sharp temperature rise in shock layer because of chemical reactions.

The numerical simulation of supersonic and hypersonic flow field around concave cavity is challenging because unlike in the case of convex and flat shape, concave shaped blunt nose has highly unsteady three dimensional flow motion in front of the body which can interact with the bow shock as well as with wake. Several attempts have been made in early researches to compute flow field around concave blunt nose. Bastianon¹³ have numerically simulated inviscid axi-symmetric flow around a concave cavity in cylindrical body immersed in supersonic flow of Mach 3.0, and found that for cavity

depth more than 40 %, flow field becomes unsteady and shows undamped periodic oscillations at frequency 740 Hz for ratio of cavity depth to body radius of 0.55. He further compared his numerical computation for cavity shape used by Cooper et al.⁸ at Mach 4.95 and found frequency of stagnation pressure as 9000 Hz, while Cooper et al.⁸ had found frequency approximately of the order of 2000 Hz. Bohachevsky et al.¹⁴ have computed unsteady inviscid flow field around cylindrical cavity in a cylinder and observed the solution reached steady state in damped oscillatory manner. The shock oscillation wavelength is 4.5 times of distance between tube base and bow shock. Sambamurthi et al.¹⁵ have investigated two-dimensional conical walled cavity with flat base at Mach 10, and predicted that bow shock oscillates approximately at fundamental acoustic frequency of the cavity, with wavelength 4 times the distance between mean shock position to base.

In later researches, the forward facing cylindrical cavity have been studied extensively as flow control method on the concept of Hartmann - Sprenger Tube¹⁶ to reduce aerodynamic heating. Huebner et al.¹⁷ have experimentally studied conical wall cavity with flat circular base at Mach 10 and determined the frequency of shock oscillations using laser interferometry and found that the oscillatory frequency is inversely proportional to cavity depth and corresponds to the fundamental acoustic frequency of cavity as in case of wave propagation in closed end cylinder. Yuceil et al.¹⁸ have experimentally studied hemispherical cylinder body with different length and diameter ratio (L/D) nose cavities at Mach 4.9 air flow. He found that for shallow cavity ($0.15 \leq L/D \leq 0.35$) or very deep cavity ($L/D \geq 1$) an axi-symmetric steady cool ring forms downstream of the lip with surface temperature lesser than model without cavity. Intermediate depth ($0.4 \leq L/D \leq 0.7$) exhibit unstable behavior in cavity pressure with higher amplitude and random fluctuations, that results in non-axisymmetric temperature field around cavity. Engblom et al.¹⁹ have demonstrated that resonant pressure oscillations, which are observed in the experiments for forward facing cavity at Mach 4.9, can occur numerically with the presence of freestream disturbance. To examine the effect of wind-tunnel noise, Ladoon et al.²¹ have studied forward facing nose cavity at Mach 4 quiet-flow wind tunnel and introduced localized controlled perturbations by laser system as thermal spot ahead of bow shock. It has been observed that for $L/D \geq 0.488$, the cavity resonate in a nearly sinusoidal manner as a damped harmonic oscillator. The cavity base pressure decay exponentially and damping constant reduces with increase in cavity depth. Further Juliano et al.²² had observed that smaller blunt sphere-cone nose at angle of attack 24° leads to starting issue in Mach 6 quiet wind tunnel under noisy flow environment, while slightly bigger model performs well during quiet operation of wind tunnel. The forward facing cavity with different L/D ratios in quiet and noisy environment have been tested and found that higher mode peak frequencies occur at integral multiple of fundamental acoustic frequency of cavity. An acoustic analogy, similar to Helmholtz resonator have been established by using numerical method for forward facing cavity receptive to freestream disturbances in supersonic flow field by Engblom et

al.²³. Ellipsoidal and parabolic nose cavities have been numerically studied by Rajesh et al.^{24,25} in hypersonic flow field to investigate aerodynamic heating and suggested that shallow parabolic cavity and ellipsoidal cavity reduces the total heat transfer rates to blunt bodies.

In above mentioned previous studies, it is evident that the cavity in front of blunt nose has advantage to reduced aerodynamic heating, but it also have unsteady flow field in the cavity, which may leads to violent bow-shock fluctuations. The flow visualization of bow shock have been performed by Hiraki et al.²⁶ for two dimensional concave cavity referred as reflector in supersonic flow. For Mach number less than 3.5, bow shock formed in front of reflector as axi-symmetric but for higher Mach number, the bow shock become highly unsteady and asymmetric. Later, Hiraki et al.²⁷ have measured force and pressure for two-dimensional concave cavity and hemispherical cavity at Mach number 4. In recent research for hemispherical concave cavity, Mizukaki et al.²⁸ have visualized large fluctuations in bow shock for supersonic Mach number higher than 3.0. The mechanism of bow-shock instability with time resolved Schlieren images have been discussed by assuming density disturbance in the cavity. Ohnishi et al.²⁹ had observed bow-shock instabilities in from of partial curved bow shock in low γ gas environment by using numerical simulations in front of edged flat surface at high Mach numbers. The critical density ratio across the bow shock have been identified as 10 to have unstable bow shock. It was stated that the slip-line near the edge plays important role for bow shock instability. Hatanaka et al.³⁰ have numerically simulated the flow field around the concave hemisphere for 50 ms at Mach 4, similar to the experiments conducted by Mizukaki et al.²⁸ and found two kind of flow configurations in bow shock. Initially bow shock oscillates in sinusoidal manner after reaching steady state. Later after 20 ms, large amplitude bow shock fluctuations appear. The mechanism of bow shock instability was explained as the component of vorticity remain in the cavity during initial sinusoidal motion of bow shock, which grows with time and produce large amplitude fluctuations.

Many of the above related researches are mainly focussed on low aerodynamic heating capability of cavity in front of blunt nose and the concave cavity have been studied in supersonic flow regimes. However, the physical phenomenon involved in large bow shock fluctuations have not been addressed with complete understanding. Moreover, to utilize the high drag configuration of concave hemispherical nose shape, it is required to control the bow shock fluctuations in front of concave shaped blunt nose. The concave cavity is not easily accessible during the experiments, hence, by studying the effects of different control methods, the information about bow shock instability mechanism can also be extracted.

1.3 Flow control Methods

Efficient flow control methods can improve or modify the performance of fluid system. Various flow control methods have been devised and studied in many applications of fluid systems to manipulate the flow field for desired behavior. In general, flow control methods can add or remove small amount of energy to the fluid systems to change its characteristics. Depending upon method of adding and removing energy from the fluid system, flow control methods can be classified in two main categories as active flow control and passive flow controls². In active flow control, an external source of energy required to provide desired flow control to the system, while in passive flow control method small temporary or permanent modification in geometry may lead to draw the energy from the system itself to provide desired flow control. The passive control method are advantageous in aerospace applications as it is not required to carry extra energy source as in case of active control methods. The effective use of passive control method require extensive understanding of flow behavior in case of geometric modifications. Some examples of active flow control methods studied in high-speed flows and some passive flow control methods, which are relevant to this thesis are discussed as follows:

1.3.1 Active Control

Active flow control methods can use fluid, acoustic, chemical or electrical energy to manipulate the flow field. Huebner et al.¹⁷ have found that the amplitude of bow shock oscillation in front of cylindrical cavity can be reduced by 70 % by injecting small amount of air in the cavity. Zhuang et al.³¹ have used supersonic micro-jets on leading edge to reduce unsteadiness of the supersonic cavity flows. Venukumar et al.³² have realized 30 - 45 % reduction in drag coefficient of blunt nose in hypersonic flow by using supersonic counter flow jet. For high bandwidth active control, powered resonance tubes, which is based on Hartmann-Sprenger tube, have been studied by Raman et al.³³. A minitature combustion driven jet with combustion volume of 1 cm^3 has been studied as active flow control method by Crittendon et al.³⁴. In hypersonic flow, drag reduction up to 50 % have been achieved by Satheesh et al.³⁵ by providing concentrated energy deposition using electric discharge. Watanabe et al.³⁶ have studied effect of direct current plasma discharge in hypersonic boundary layer.

1.3.2 Passive Control

The flow field manipulation by small modification in geometry leads to add or remove energy from the fluid system to have desired control. Many passive flow control methods have been studied in high-speed flows with application from drag reduction device in blunt nose to mixing promoters and noise reduction in high-speed jets. Concave shape itself is kind of passive control method, which can have

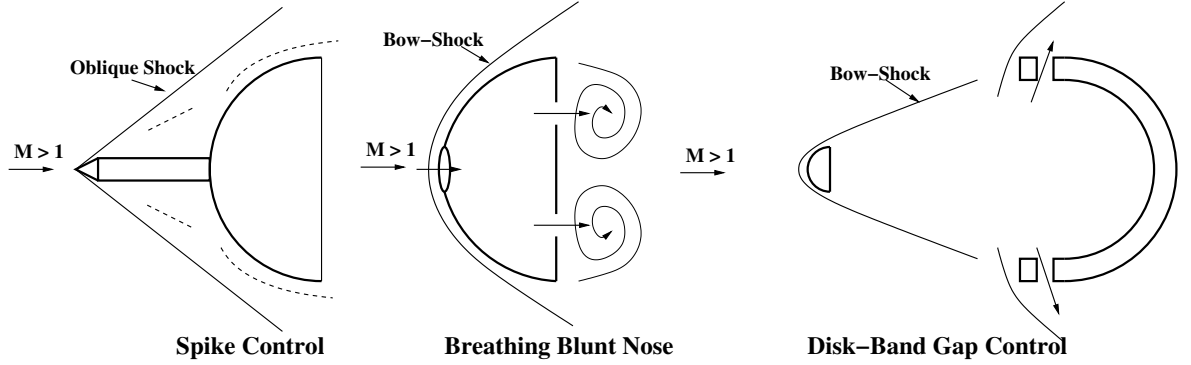


Figure 1.3a: Various passive flow control for upstream flow

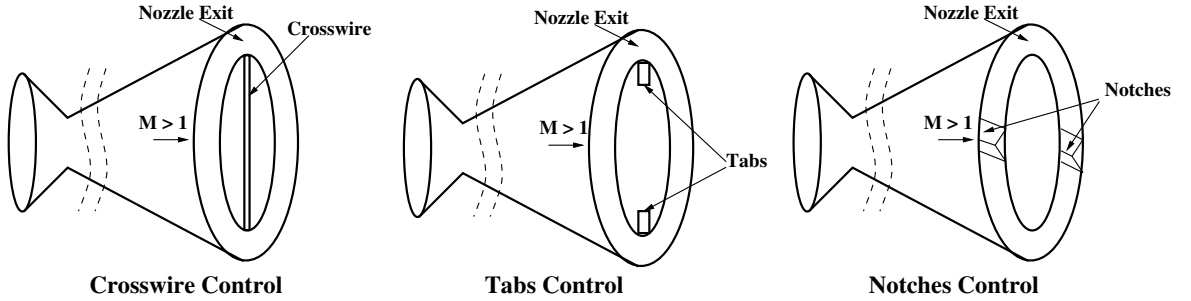


Figure 1.3b: Various passive flow control for jets

higher drag and better heat transfer in comparison to same cross-sectional area of convex shape blunt nose, which makes concave shape useful for hypersonic decelerator to use during atmospheric entry. Figure 1.3a shows schematic of different passive control methods studied for flow control in front of the bodies. Khurana et al.³⁷ have studied application of aero-spike to reduce drag for lifting body surfaces by moving bow shock wave away from the blunt nose body. The effectiveness of breathing blunt nose (BBN) concept for drag reduction have been demonstrated by Imamura et al.³⁸ in hypersonic flow. Breathing blunt nose allows high pressure in front of the blunt nose to pass through the base of the body, which leads to reduction in bow shock strength near location of breathing hole and increase in the base pressure. Hence, breathing blunt nose can effect front as well as base flow. Later, Watanabe et al.³⁹ have studied the aerodynamic characteristics of breathing blunt nose at hypersonic Mach number 7. Vashishtha et al.⁴⁰ have investigated the effectiveness of breathing blunt nose at supersonic speed. The performance of disk-band-gap for supersonic parachute model was investigated by Wernet⁴¹. The disk-band-gap flow control allows part of the flow coming to the supersonic parachute cavity to pass through the side gaps. Many passive flow control devices have been studied for subsonic and supersonic jet control to enhance mixing or to suppress the noise generated by jets in many applications. Figure 1.3b represents schematic of some of the passive control methods used for subsonic and supersonic jet control. The effectiveness of tabs to enhance jet mixing have been studied by Clement et al.⁴². The tabs can introduce streamwise small vortices in the shear layer which can promote mixing in the jet field. However, Rathakrishnan⁴⁴ have found that the limit of length of tabs as mixing enhancer

was upto the radius in form of crosswire. It means the jet mixing can enhanced by introduction of small vortices not only in the shear layer but across the nozzle exit. Notches at the exit of nozzle lip can also modify the jet flow field. Verma et al.⁴³ have experimentally studied the effect of notches in circular slot underexpanded jet to reduce the noise field and found that notches can reduce far field shock associated noise in jet field. Hence, small modification in the geometry can lead to adding or removing small disturbances to the flow field, which can manipulate the flow field for desired output.

1.4 Need for study of Bow-Shock Instability and Control

In early researches, it was found that cavity in front of blunt nose in supersonic and hypersonic environment have reduced aerodynamic heating with steady bow shock. The unsteady motion of bow shock leads to even more reduced heating in wind tunnel test conditions. The drag coefficient of concave shaped blunt nose is higher than the conventional convex shape blunt nose. These two characteristics of concave shaped blunt nose, makes it suitable to utilize as hypersonic decelerator. However, large amplitude fluctuations in bow shock can lead to fluctuations in aerodynamic forces as well as heat transfer coefficients and flow physics behind these large amplitude bow shock fluctuations is not clearly understood. There can be many reasons for these violent fluctuations in bow shock e.g. upstream flow non-uniformity, structural oscillations of geometry, particle induced instability or aerodynamic instability because of bow-shock and cavity vortex interactions or bow shock and reflected disturbance wave interactions.

In previous experimental studies, main focus was given to measurement of pressure and heat transfer coefficients in front of cylindrical cavity in supersonic and hypersonic flows. However, the quantification of large amplitude bow shock fluctuations and its effect on aerodynamics forces are not measured in hypersonic flows. Hence, it is required to quantify the unsteady bow shock behavior and its effect on aerodynamic forces. To quantify the bow shock fluctuations, it is proposed to utilize the time resolved flow visualization method by using high-speed camera and further using image processing methods to obtain time series data of shock fluctuations.

Further, to understand the bow shock fluctuations in front of concave shape geometry, it is also necessary to understand the reasons of very stable bow shock in front of conventional convex and flat blunt nose with respect to disturbances in the flowfield. A typical behavior of bow shock in front of convex or flat shaped blunt noses as stable bow shock or bow shock fluctuating at high frequency and small amplitude. Hence, it can be proposed that the bow shock oscillations in front of conventional convex blunt nose behaves as linear damped harmonic oscillator with respect to small perturbations in freestream. Figure 1.4a shows the mean shock position in front of convex hemispherical blunt nose, which can be expressed by the following relation⁴⁵:

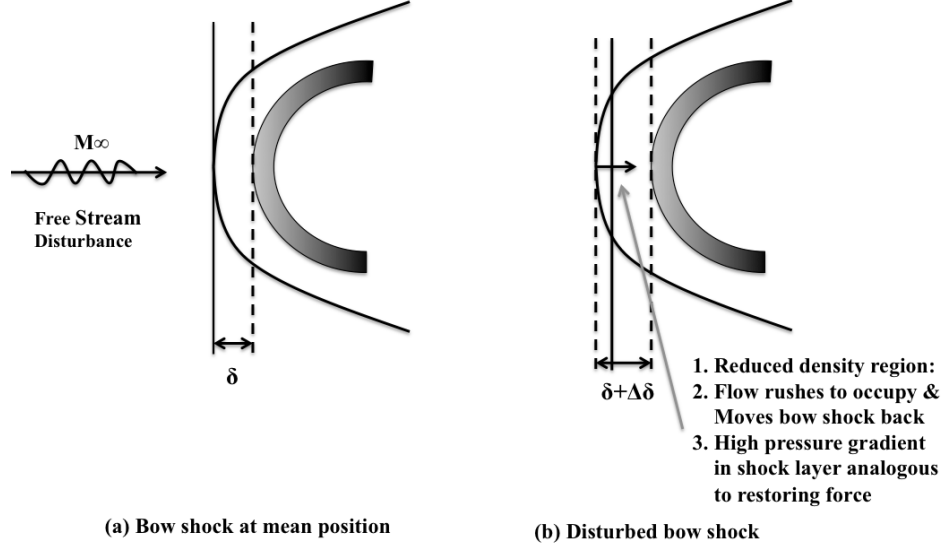


Figure 1.4: Disturbance in bow shock in front of conventional convex blunt nose

$$\frac{\delta}{D} = \kappa \frac{\rho_{\infty}}{\rho_s} \quad (1.1)$$

where, δ is mean shock stand off distance along the centerline, D is diameter of the hemisphere, ρ_{∞} is freestream density, ρ_s is density immediately behind the bow shock and κ is constant, which depends on blunt nose geometry. Lobb⁴⁵ has found experimentally that the value for κ is 0.41 for spheres in air. As the central region of bow shock is almost normal shock, the relation of density ratio can be expressed in terms of Mach number M and specific heat ratio γ from normal shock relations² and Eq. 1.1 can be expressed as follows:

$$\frac{\delta}{D} = \kappa \frac{(\gamma - 1)M_{\infty}^2 + 2}{(\gamma + 1)M_{\infty}^2} \quad (1.2)$$

Equation 1.2 shows that the shock stand off distance for a particular size and shape of blunt nose, depends on specific heat ratio γ and freestream Mach number. For air flow, the specific heat ratio can be constant for thermally perfect gas limit, and small perturbations in freestream Mach number can induce damped oscillatory motion in bow shock. Figure 1.4b shows slightly disturbed position of bow shock (moved away from the body) because of some freestream disturbance, which leads to reduced density region and reduced pressure gradient in the shock layer. The upstream flow with higher momentum will rush to occupy the region. This will result in the bow shock to move back towards its original position and pressure gradient again rises. However, the viscous dissipation in the shock layer can be analogous to damping, which will damp the bow shock motion further. The damped harmonic oscillations of bow shock, which can be excited by external disturbances can be

described by following equation:

$$\ddot{\delta} + 2\zeta\dot{\delta} + \omega_0^2\delta = \varepsilon\cos\Omega t \quad (1.3)$$

where, δ is bow shock stand off distance near the centerline, ζ is damping ratio, which is analogous to viscous dissipation in shear layer, ω_0 is natural frequency of shock oscillation, depends on the restoring force, which can be analogous to high pressure gradient in the shock layer, which again dependent on the freestream flow conditions. ε is small amplitude of freestream disturbances and Ω is excitation frequency of freestream disturbances and t is time. In case of convex shape geometry, freestream disturbances can be dissipated in thin shock layer easily and because of thin shock layer, the pressure gradient in shock layer can be very high. Hence, the bow shock fluctuations in front of convex shape geometries can be highly damped. However, same size of concave shape geometry can influence the pressure gradient in shock layer as the extent of shock layer increases inside the concave cavity, which may have severe effect on bow shock. Hence, it is required to develop understanding of violent the bow shock fluctuations in front of concave shape geometry from the frontal shock layer dynamics point of view.

To utilize the concave shape geometry as hypersonic decelerator, it is also required to provide the flow control method to make bow shock stable by manipulation of vortices in and around the concave cavity. The passive control methods can be advantageous over active control methods to control the bow shock in front of concave shape geometry. Hence, few passive flow control methods (schematic shown in Fig. 1.5) have been utilized in this study to accomplish two objectives, one is to study the effectiveness of these different flow control methods and second is to strengthen the understanding of bow shock fluctuation mechanism by understanding the effect of small geometric modification in concave shaped blunt nose. These passive flow control methods are inspired from the previous studies of different passive flow control methods in high-speed flows as discussed in section 1.3.2. Figure 1.5, shows the configuration of these passive control methods for concave shaped blunt nose in form of flat base or hemispherical cavity in cylinder, notch control, tab control, breathing control, spike control and crosswire control. These passive control methods are chosen based on basic understanding that the large fluctuations in bow shock may be because of unsteady flow motion inside the cavity, which may result in reverse flow from the cavity towards the bow shock. The flat base control can reduce the slip line fluctuations, which is formed at the edge of concave hemispherical shell and oscillate because of flow separation on the curved base. This may reduce the unsteadiness in the flow inside the cavity. The notch control may allow the unsteady disturbances inside the cavity to move away from the edges. The tab control can provide control in shear layer by introducing small eddies from its surface, which may reduce the strength of large size vortical flow. The breathing control can allow the high pressure

in the cavity to move out to the base, which may lead to reduced fluctuations in bow shock. The spike control can stop movement of large flow structure in cavity at the center, while crosswire can partially stop the disturbances to enter the cavity and also introduce small eddies through out the diameter of the cavity to reduce large vortical motion inside the cavity.

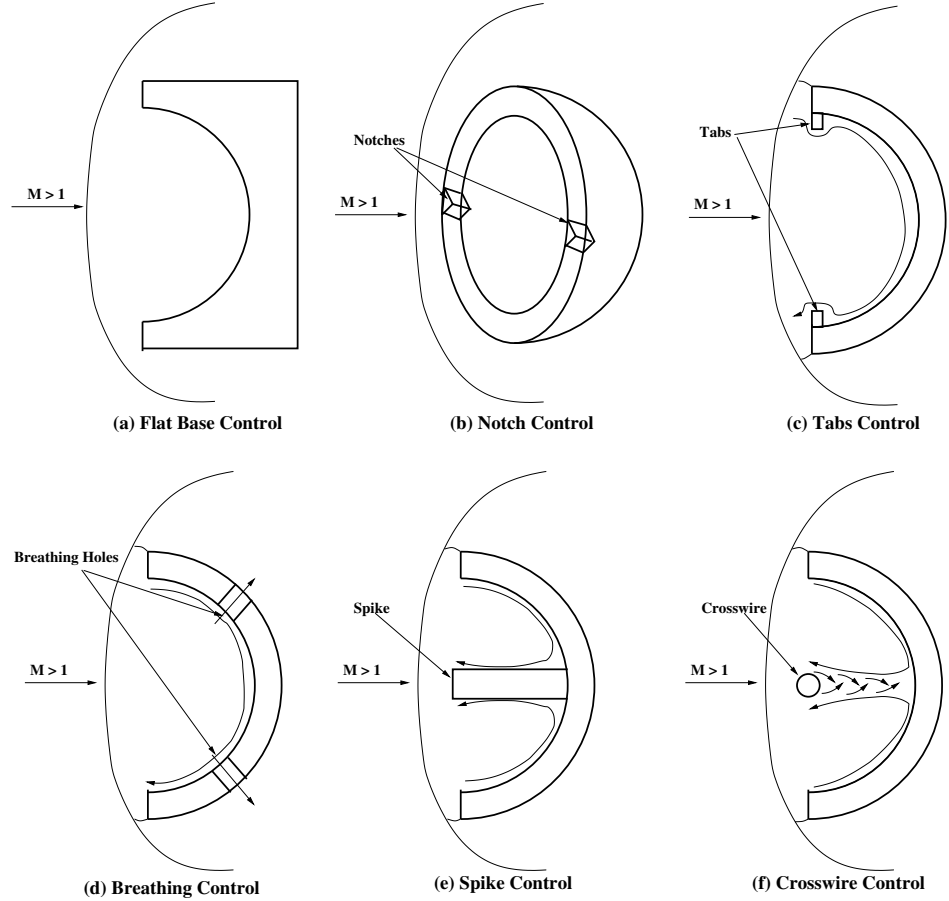


Figure 1.5: Schematic of Passive flow control methods devised in this study to concave shaped blunt nose

Further, three dimensional numerical simulations of flow field around concave shaped blunt nose can provide the more information regarding flow physics inside the cavity, which is inaccessible in experimental studies. In several numerical studies, the two dimensional, axi-symmetric flow field around cylindrical cavity and concave cavity have been simulated and damped oscillatory nature of bow shock have been found. Hence, it is required to compute three dimensional flow field around the concave shaped blunt nose to have better understanding of flow physics. Large amplitude bow shock fluctuations have not been reported in numerical simulations with uniform freestream flows until recently, by Mizukaki et al.³⁰. He had reported large amplitude bow shock fluctuations as visualized in supersonic flow field in front of concave hemispherical shape by computing for longer time, but

the system becomes unstable with rapid bow shock movement. Hence, it is challenging to develop numerical methods to understand the flow physics behind the bow-shock fluctuations.

1.5 Objectives

To realize the concave shape blunt nose as hypersonic decelerator, this research study has following main objective:

- To understand the flow physics of bow shock instabilities in front of concave shape blunt nose.
- To provide effective passive flow control method to stabilize the bow shock in front of concave shaped blunt nose as well as to strengthen the understanding of bow shock instabilities by studying the effects of diverse passive flow control methods.

Initially, flow visualization of bow shock fluctuations and measurement of aerodynamic forces around circular flat, convex and concave hemispherical shaped blunt nose have been performed at Mach number 7 in hypersonic wind tunnel test-section. The bow shock fluctuations have been quantified and analyzed by measuring bow shock displacements by using image processing method from the time resolved flow visualization video. Further, different passive flow control methods were employed for concave blunt nose and effects of these passive control methods were studied by force measurement and shock displacements from flow visualization methods. Later, to understand the three dimensionality of bow shock fluctuations, numerical simulations were performed for wind tunnel test-section conditions for circular flat, convex and concave hemispherical shell geometries. However, the concave shape simulations becomes unstable, when there is large bow shock movement, the onset of bow shock fluctuations are analyzed from three dimensional flow field around the concave geometry and the mechanism of large bow shock fluctuations is explained. The objective of numerical simulation is not to replicate the experimental bow shock large deformation patterns, but to have an understanding of unsteady flow field inside the cavity, which leads to large bow shock fluctuations. The process to achieve above stated objectives can be summarized as follows:

1. Establish the experimental analysis method for bow shock instability in front of flat circular, convex and concave shaped blunt nose by force measurement, flow visualization and image processing techniques.
2. Employ the passive flow control methods for concave hemispherical shell to analyze their effects on bow shock instability. Draw reasoning from studying of these passive flow control methods for bow shock instability mechanism.

3. Explain the three dimensional flow motion around the concave shape geometry and mechanism of onset of large bow shock fluctuations by numerical simulations.

1.6 Outline of Thesis

In chapter 2, the details of experimental facility, method for force measurement and flow visualization are discussed along with data processing technique by method of image processing from high-speed flow visualization video and estimation of freestream disturbances is also explained.

In chapter 3, the experimental results for circular flat, convex and concave shape hemispherical shell are discussed by force measurement, bow shock displacement time series and proper orthogonal decomposition for concave hemispherical shell. Further, the effect of change in angle of attack in front of concave shaped blunt nose is discussed by force analysis and shock displacement along centerline.

In chapter 4, the experimental results for passive flow control methods on concave hemispherical shell are discussed and further understanding of bow shock instability mechanism is developed.

In chapter 5, numerical methods utilized for computing three dimensional flow field around flat, convex and concave shape blunt nose are discussed.

In chapter 6, the numerical results are discussed for hypersonic flow field around the flat, convex and concave shaped geometries. The mechanism of onset of large amplitude bow shock fluctuations is discussed for concave hemispherical shell.

In chapter 7, the bow shock instability in front of concave shape have been discussed with the understanding developed by experimental studies and numerical studies.

In chapter 8, the results are concluded.

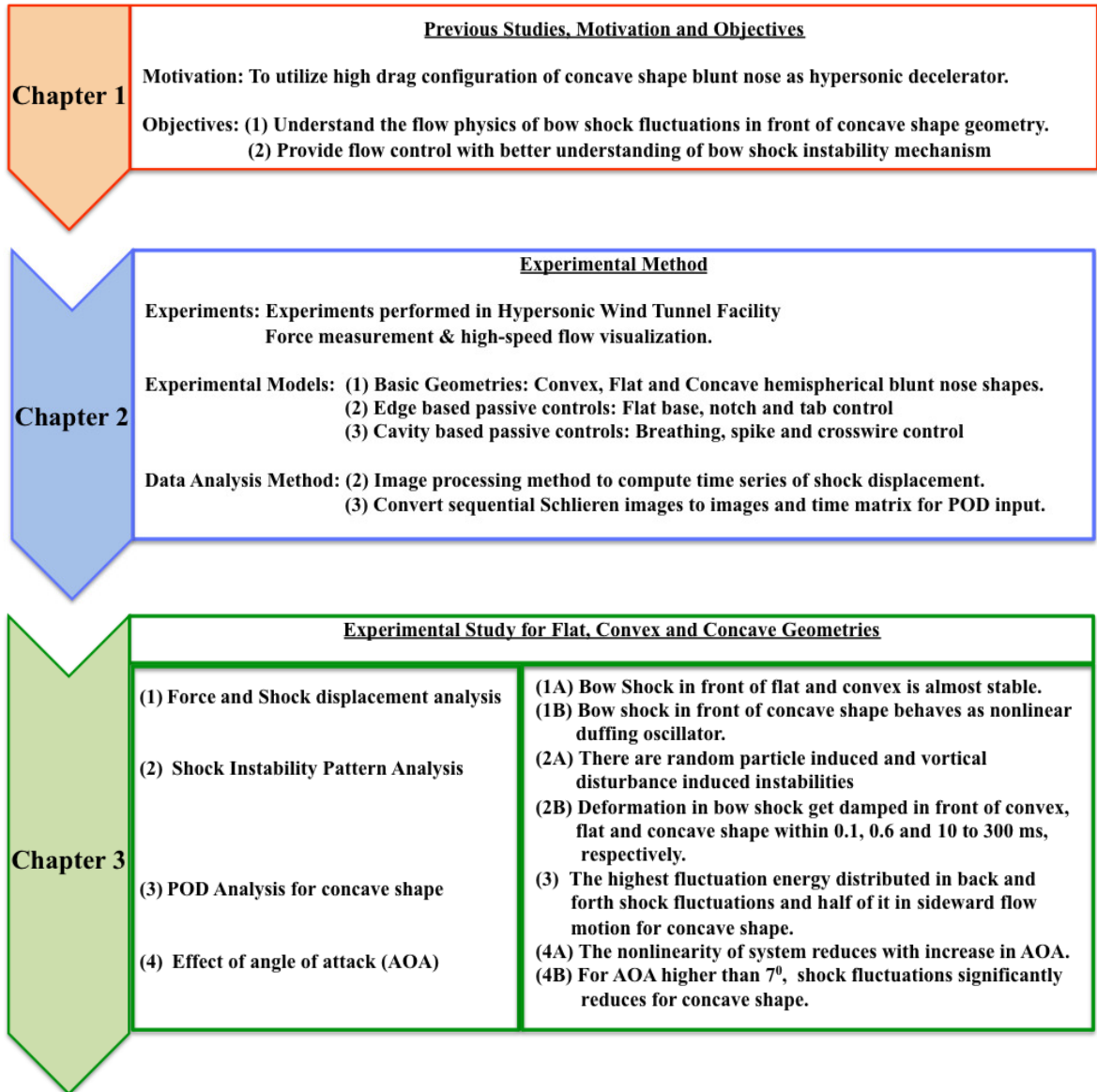


Figure 1.6a: Road Map of the study

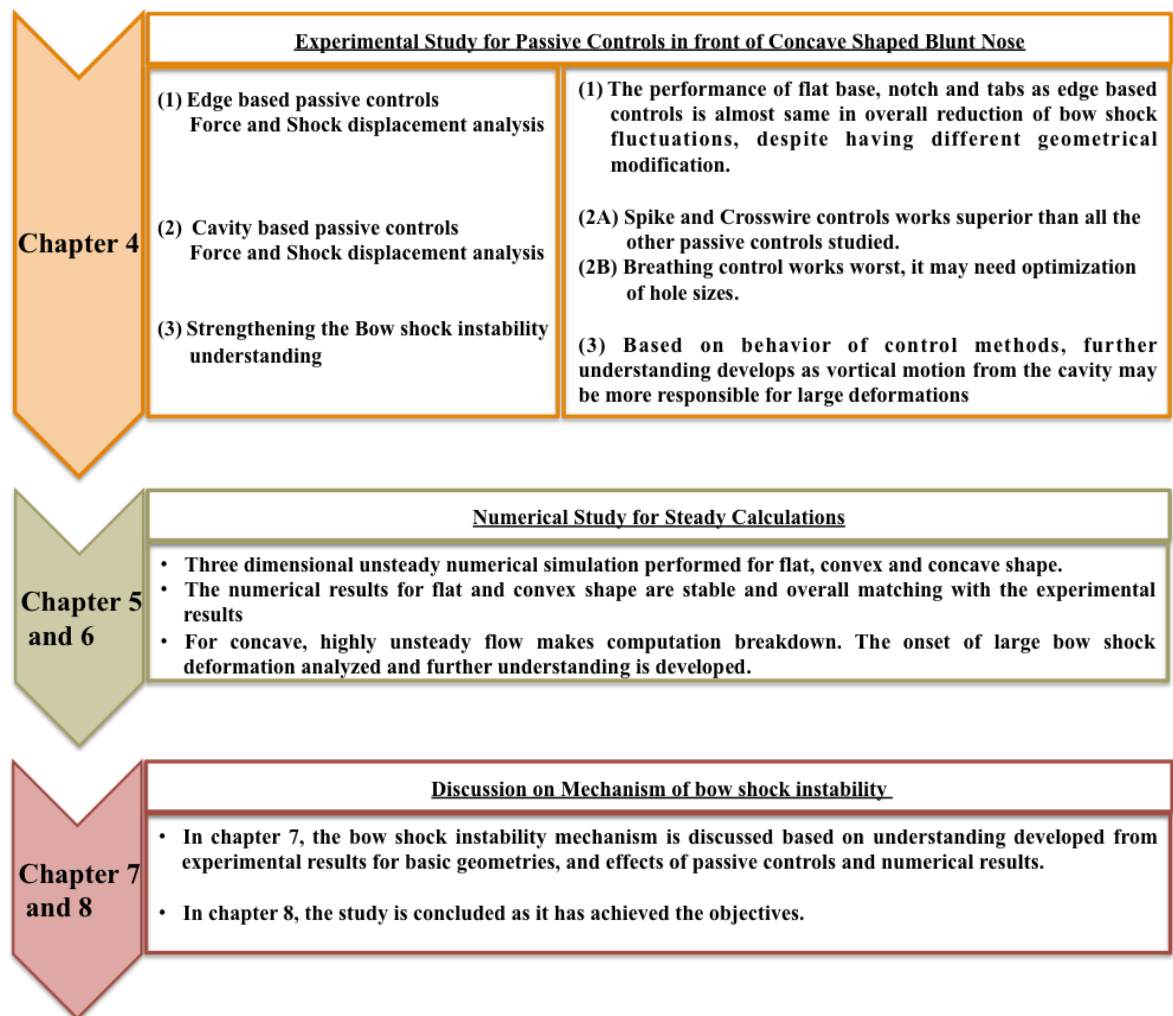


Figure 1.6b: Road Map of the study (continued)

Experimental Study

Chapter 2

Experimental Methodology

2.1 Hypersonic Wind Tunnel Facility

2.1.1 Wind Tunnel Specifications

In this study, all the experiments were carried out at Kashiwa Hypersonic and High Enthalpy Wind Tunnel facility situated at Kashiwa Campus, The University of Tokyo. This facility has two sections for two mode operations: one section is for high-speed flow (hypersonic wind tunnel) and another section is for combustion tunnel (high enthalpy flow). In this study, the experiments are performed at hypersonic wind tunnel section. The flow characteristics for hypersonic flow in wind tunnel test-section were studied by Imamura et al.⁴⁶. The pictorial view of Hypersonic facility along with test-section view is shown in Fig. 2.1. The general specifications of hypersonic wind tunnel are listed in Table 2.1. The hypersonic wind tunnel can operate at Mach Number 7 and 8. The stagnation pressure can

Table 2.1: Hypersonic Wind Tunnel Specification⁴⁶

Property	Specification
Mach Number	7.0, 8.0
Stagnation Pressure	Maximum 0.950 MPa
Stagnation Temperature	Maximum 1000 K
Mass Flow Rate	Maximum 0.39 kg/s
Nozzle Exit	200 mm diameter, with uniform core of 120 mm diameter
Unit Reynolds Number	1.0×10^4 1/cm
Run Time	Maximum 60 sec.
Reservoir	5 MPa (G), 4 m^3 (x1)
Heater	Pebble-type + city gas burner
Exhaust	Vacuum tank (7 m diameter)

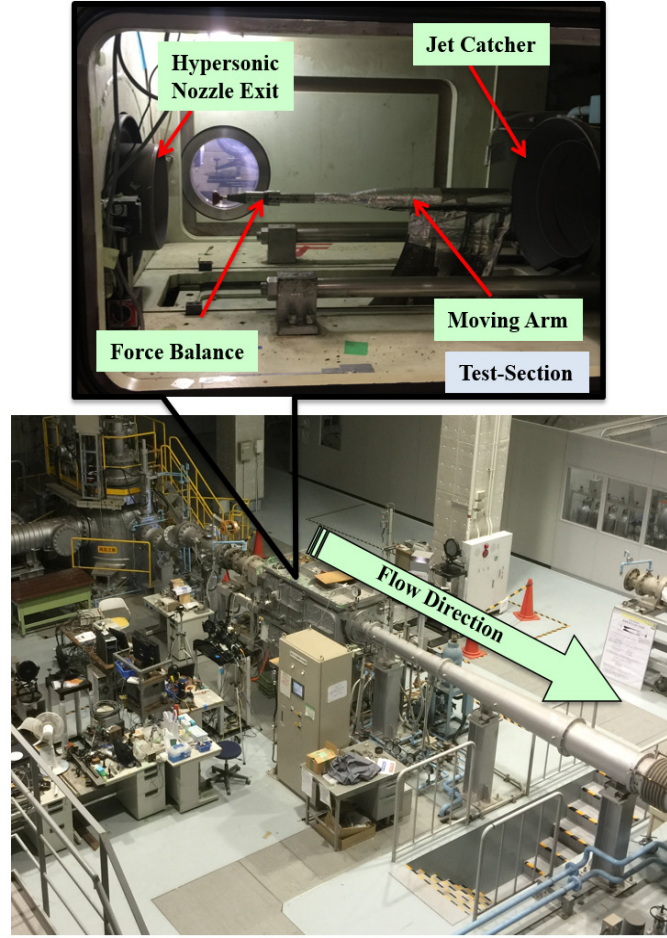


Figure 2.1: Pictorial view of hypersonic wind tunnel facility and test-section

reach up to maximum approximately 950 kPa and stagnation temperature can reach up to maximum approximately 1000 K. The mass flow rate through the nozzle is maximum 0.39 kg/s. The high temperature and high pressure air is maintained in pebble-type city-gas heater, which is ejected by opening hot shut-off valve, through the hypersonic nozzle in the test-section. Further, the flow is evacuated in the vacuum tank connected by the jet catcher in the test-section. The exit diameter of hypersonic nozzle is 200 mm, which can provide 120 mm core hypersonic flow. The maximum run time for the hypersonic flow in the test-section is 60 seconds. The unit Reynolds number of the flow field is 1.0×10^4 /cm, which is relatively smaller as compare to other hypersonic flow facilities. The pictorial view of test-section is shown in Fig. 2.1 (top image). The experimental model is connected to a moving arm in front of hypersonic nozzle. During the experiments, the experimental model is inserted in the hypersonic flow field after the hypersonic flow is established in the test-section, and later moved out after completion of measurements and before end of hypersonic flow. To perform the flow visualization, the test-section have transparent side and top windows.

2.1.2 Instrumentation for Force Measurement

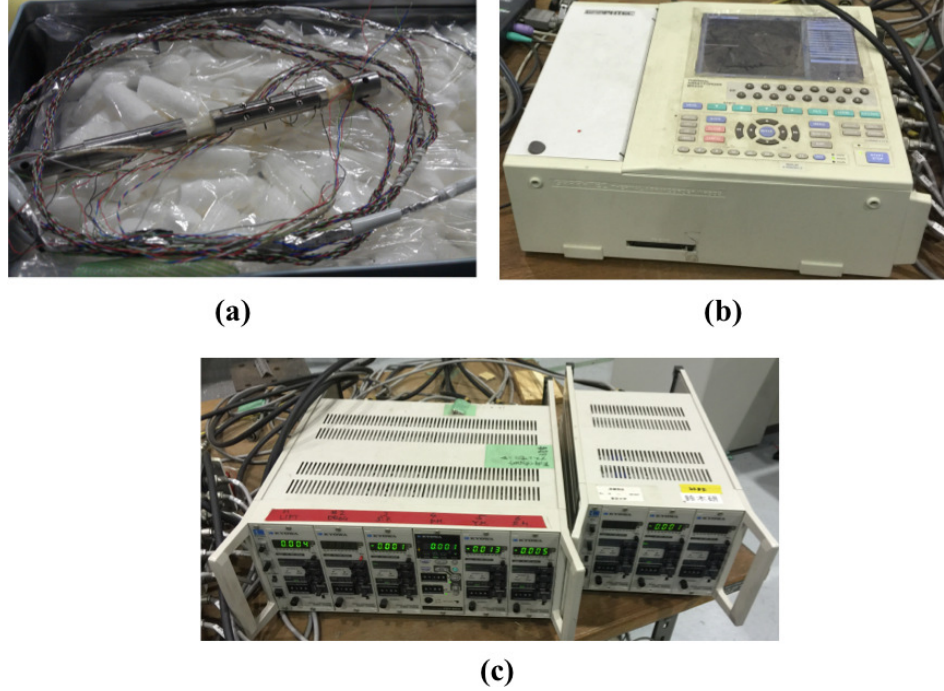


Figure 2.2: Force measurement instrumentation (a) Force Balance, (b) Data Logger, (c) Signal Conditioner

The wind tunnel facility provides a six component force balance system for the measurement of normal, axial, side forces and pitching, yawing and rolling moments in hypersonic flow field. The force measurement system consists of force balance, data logger and signal conditioner. The pictorial view of the force balance is shown in Fig. 2.2a. The force balance has six strain gauges, which is based on wheat-stone bridge circuits. The output voltage from each strain gauge is conditioned using KYOWA CDV-700A constant voltage signal conditioner (shown in Fig. 2.2c), further the voltage data was recorded using data logger, Graphtec Thermal Arraycorder WR300 as shown in Fig. 2.2b. The data logger also records stagnation pressure, stagnation temperature, test-section pressure, angle of attack along with six component of forces and moments. However, it can record maximum 16 outputs simultaneously. The force balance is attached to moving string in the wind tunnel test-section and the experimental model is connected to the force balance by a mount attached to force balance. The signal conditioner provides the input voltage of $\pm 1V$ for strain gauges of force balance and returns amplified output voltage ($\pm 10V$) by converting measured strain to voltage, which is further recored by data logger.

2.1.3 Optical System for Flow Visualization

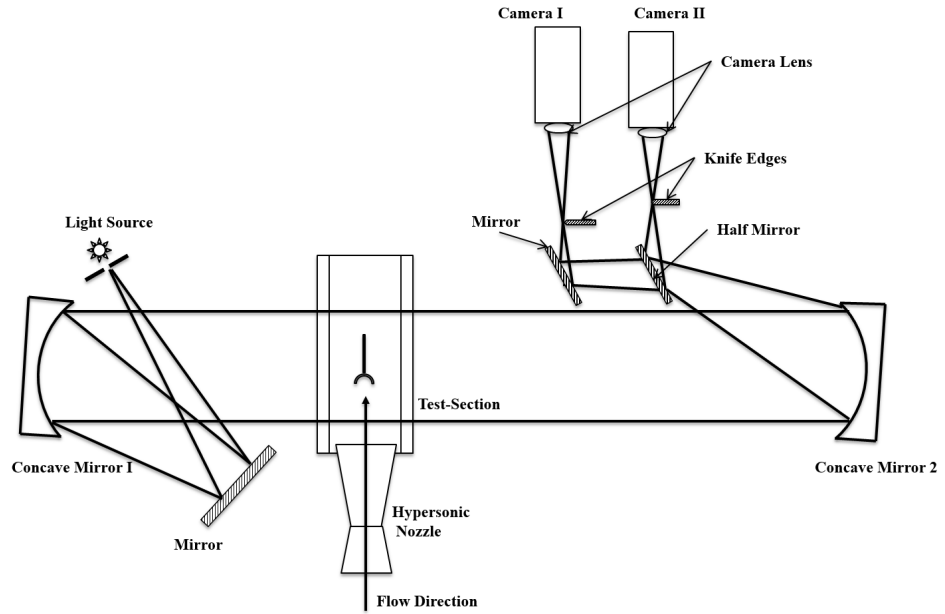
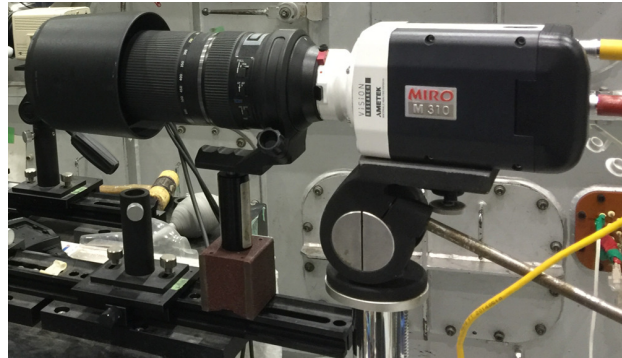


Figure 2.3: Schematic representation of twin mirror Schlieren system



(a) Light Source



(b) High Speed Camera

Figure 2.4: Pictorial view of (a) Light Source (b) High speed camera with lens

High-speed optical visualization methods are based on principle that light ray bends or refracts when it passes through variable density medium. Basic Schlieren system consists of light source, concave mirror, knife edge and camera. The output image from Schlieren system corresponds to first derivative of density. A twin mirror Schlieren system is available at hypersonic wind tunnel facility. The schematic of the same is shown in Fig. 2.3, which uses two identical concave mirrors. The light rays coming from light source, are directed to concave mirror by using one smaller mirror placed at the focal point of the concave mirror to make it parallel. After reflecting from concave mirror the light

rays pass through the test-section from the side windows and reach to the second concave mirror at the other end. From the second concave mirror, light rays reach to a half mirror, which allows half the light to direct towards the one camera and other half towards the another mirror. The second mirror directs the light rays towards the another camera. Before reaching both the cameras, the knife edge is placed between mirrors and camera to cut the half light in horizontal or vertical direction depending on the kind of shock wave visualization. In the current experiments, bow shock is visualized by keeping knife edge position as vertical. Xenon lamp with power supply (model XB10201 AA-A) is used as light source. The pictorial view for the same is shown in Fig. 2.4a. In general, a high resolution still camera and a CCD video camera is used during the experiments. In this study, a high-speed camera to record time -resolved Schlieren video is integrated with the current Schlieren system, by replacing the still camera with Phantom MIRO 310 high-speed camera and TAMRON A011 high zoom lens system. The pictorial view for high-speed camera with lens system attached is shown in Fig. 2.4b.

2.2 Experimental Models

All the experimental models were manufactured from Bakelite material, which has good mechanical strength and heat resistive properties. The experimental models were fabricated by using 3-D rapid prototyping milling machine Roland MODELA MDX-540A, which can fabricate models with spatial accuracy of ± 0.05 mm with the milling drills of 3 mm diameter installed. The input for the rapid prototyping machine is three dimensional CAD data, which was prepared using Autodesk Inventor (R) 2011. The experimental models manufactured and studied in this study can be divided in two parts: basic geometries and passive flow control geometries. All the geometry have same cross sectional diameter as 30 mm.

2.2.1 Basic Geometries

A circular flat plate, convex and concave hemispherical shell geometries have been fabricated as basic geometries for flat blunt nose, convex blunt nose and concave blunt nose shapes, respectively. The three dimensional CAD geometry and other geometrical details in sectional view for basic geometries are shown in Fig. 2.5. All the geometries have maximum outer diameter of 30 mm. The length of each geometry is 20 mm. In wind tunnel test-section, maximum size of experimental model which can be tested is approximately 50 mm. The base diameter of experimental models was selected as 30 mm because unsteady motion of bow shock wave in front of bigger size concave shape may break the flow field in the test-section from starting, which was experienced earlier in case of studies of concave shape arc as reported by the same author⁴⁷. The thickness of each geometry is used as 3 mm, which gives 12 mm diameter front cavity in case of concave shape hemispherical shell. At the base of

Note:

This is abridged version of doctoral thesis.

Further contents of Chapter 2 are planned to be part of published Journal articles in future.

The pages 27 - 45 in Chapter 2 will be open to public after September 16, 2021.

Chapter 3

Experimental Results for Basic Geometries

3.1 Outline

In this chapter, first the results of flat circular, convex and concave shaped blunt noses are discussed for zero angle of attack experiments by analyzing force coefficients, shock displacements. The analysis of time history of bow shock displacements provide information of nonlinear fluctuations in front of concave shape geometry. Further, particle induced patterns of bow shock fluctuations in front of convex and flat geometry are discussed by using sequential Schlieren images. By using the time stamps from bow shock displacement plots and sequential Schlieren images, the initiation of large deformation of bow shock because of vortical disturbance in free stream, in front of concave shaped geometry is captured. Further the bow shock deformation pattern is discussed for the same sequence. However, the bow shock displacements can only provide information regarding large deformation of bow shock in front of concave shaped blunt nose in one direction, hence, large deformation in bow shock in front of concave shape blunt nose is analyzed by proper orthogonal decomposition by using Schlieren images captured from high-speed camera, which can give information regarding the high fluctuation energy modes. In the last, the effect of angle of attack is analyzed for concave shape geometry by force analysis and bow shock displacement analysis. It is found that at higher angle of attack, the bow shock becomes stable. The critical angle of attack is found, above which the bow shock remains stable. However change in angle in attack leads to higher lift force for the geometry.

Note:

Further contents of Chapter 3 are planned to be part of published Journal articles in future.

The pages 47 - 85 in Chapter 3 will be open to public after September 16, 2021.

Chapter 4

Experimental Results for Passive Flow Controls

4.1 Outline

As it is discussed in previous chapter that the transition of bow shock from stable state to large deformation state in front of concave shaped blunt nose may be caused by external disturbances, which can get swallowed inside the cavity and excite the flow to have large amplitude movement. Further, the Schlieren image POD modes suggests that the back and forth flow mode and sideways flow (vortical motion from cavity to base of concave geometry) modes during large deformations of bow shock have higher fluctuation energy. Further higher POD modes are coupled because of nonlinearity of the system. It may be possible that by controlling one mode, the other mode may get effected by using passive control method. Further, understanding the effects of passive control methods for these two modes may give more insight on the the bow shock instability phenomenon. Hence, the study of passive control methods is divided into two parts as edge based passive control and cavity based passive control.

In this chapter, the experimental results for two configuration of passive flow control methods: edge based passive control as flat base, notch and tab controls and cavity based passive control methods as breathing, spike and crosswire have been analyzed. The effectiveness of different passive control methods have been assessed by analyzing the force measurement data and shock displacements along centerline, upper edge center and lower edge center. The probability density and cumulative distribution functions are compared with same for concave shape without any control. The performance of flow control method can be evaluated from the cumulative distribution function near the first peak

location along all three horizontal lines as performance index (η):

$$\eta(\%) = \Sigma p(\delta_A = 0.26) \times \Sigma p(\delta_B = 0.32) \times \Sigma p(\delta_C = 0.26) \times 100 \quad (4.1)$$

where $\Sigma p(\delta)$ is summation of probabilities from 0 to δ or cumulative distribution at δ along horizontal lines passing through upper edge center (δ_A), cavity center (δ_B) and lower edge center (δ_C). The above values of δ are chosen, as maximum small amplitude fluctuation at the stable position. It will give the approximate idea of effectiveness of flow control method. The 100 % performance means the bow shock will always remain at its stable location along centerline, upper and lower edge center. For concave shaped blunt nose without control the value for η is 5.78 %. It means that the bow shock will always remain close to the body (below the above δ values) atleast for 5.78 % time duration. Further, it is found that the spike and crosswire control methods perform better among all the passive control method studied. Hence, proper orthogonal decomposition method is applied to these two flow control method and first six POD modes are analyzed.

4.2 Edge based Passive Flow Controls

Three edge based passive control methods have been studied as flat base, notch control and tab control to control large deformation in bow shock in front of concave shaped blunt nose. The concave hemispherical shape of blunt nose have curved base. The shear layer along the curved base is oscillatory in nature and may produce alternating vortices in the wake depending on the Reynolds number of the flow. A slipstream can be formed at the edge, which may get effected because of oscillatory wake²⁹. The curved base may have higher amplitude oscillation in slipstream than the flat base. Hence, flat base geometry is studied to understand the effect of slipstream fluctuations on bow shock instability in front of hemispherical cavity. Further, notch and tab control methods are studied with notches fabricated and tabs attached at diametrically opposite locations at the edges of cavity, only in one direction. The experiments were performed by keeping the diametric line along which tabs are added or notches are fabricated, perpendicular to flow field along side force direction. Notches can allow, the vortical motion of flow inside the cavity to escape from the sides, as there will be higher pressure in the cavity and low pressure outside. The sharp edges of notches can also create small eddies during the large deformation of bow shock, which can dissipate the energy of excited flow in the cavity easily. Usually, the tabs are used to generate streamwise vortices in the shear layer to promote mixing in case of jets. Here, the tabs may work as local hindrance to freestream disturbances and during large deformation of bow shock, it can also introduce small eddies in the shear layer to enhance mixing in the cavity that may lead to reduce the strength of vortical flow motion on the cavity. The effectiveness

Note:

Further contents of Chapter 4 are planned to be part of published Journal articles in future.

The pages 88 - 115 in Chapter 4 will be open to public after September 16, 2021.

Numerical Study

Chapter 5

Numerical Methodology

The experimental results are discussed based on two dimensional image plane captured during the wind tunnel experiments and the flow field inside the cavity is inaccessible in the experiments. To further develop understanding the flow phenomenon in and around the concave shaped blunt nose in three dimension, numerical computations have been performed for wind tunnel test conditions. In this chapter, the numerical methodology used for computing flow field around three basic geometries has been described.

5.1 Governing Equations

5.1.1 Unsteady Compressible Navier Stokes Equations

The conservative form of three dimensional unsteady laminar Navier Stokes equations can be written in cartesian coordinate system (x, y, z) as follows⁵⁸:

$$\frac{\partial \mathbf{Q}}{\partial t} + \frac{\partial \mathbf{E}}{\partial x} + \frac{\partial \mathbf{F}}{\partial y} + \frac{\partial \mathbf{G}}{\partial z} = \frac{\partial \mathbf{E}_v}{\partial x} + \frac{\partial \mathbf{F}_v}{\partial y} + \frac{\partial \mathbf{G}_v}{\partial z} \quad (5.1)$$

$$\mathbf{Q} = \begin{bmatrix} \rho \\ \rho u \\ \rho v \\ \rho w \\ e \end{bmatrix}, \quad \mathbf{E} = \begin{bmatrix} \rho u \\ \rho u^2 + p \\ \rho uv \\ \rho uw \\ (e + p)u \end{bmatrix}, \quad \mathbf{F} = \begin{bmatrix} \rho v \\ \rho uv \\ \rho v^2 + p \\ \rho vw \\ (e + p)v \end{bmatrix}, \quad \mathbf{G} = \begin{bmatrix} \rho w \\ \rho uw \\ \rho vw \\ \rho w^2 + p \\ (e + p)w \end{bmatrix} \quad (5.2)$$

$$\mathbf{E}_{\mathbf{v}} = \begin{bmatrix} 0 \\ \tau_{xx} \\ \tau_{xy} \\ \tau_{xz} \\ \beta_x \end{bmatrix}, \quad \mathbf{F}_{\mathbf{v}} = \begin{bmatrix} 0 \\ \tau_{yx} \\ \tau_{yy} \\ \tau_{yz} \\ \beta_y \end{bmatrix}, \quad \mathbf{G}_{\mathbf{v}} = \begin{bmatrix} 0 \\ \tau_{zx} \\ \tau_{zy} \\ \tau_{zz} \\ \beta_z \end{bmatrix} \quad (5.3)$$

where, \mathbf{Q} is the vector of conservative variables, \mathbf{E} , \mathbf{F} and \mathbf{G} are inviscid terms and $\mathbf{E}_{\mathbf{v}}$, $\mathbf{F}_{\mathbf{v}}$, and $\mathbf{G}_{\mathbf{v}}$ are viscous terms. u, v and w are velocities in x, y - and z -directions, respectively. ρ is density, p is pressure and T is temperature, e is total energy per unit volume and t is time.

The equation of state of perfect gas is as follows:

$$p = \rho RT \quad (5.4)$$

where R is a gas constant. The static pressure p is calculated from perfect gas Equation 5.4 as:

$$p = (\gamma - 1) \left[e - \frac{1}{2} \rho (u^2 + v^2 + w^2) \right] \quad (5.5)$$

where γ ratio of specific heats and used as 1.4 for air in this study.

The shear stress components τ_{ij} forms viscous stress tensor. It can be given as

$$\begin{aligned} \tau_{xx} &= \lambda(\nabla \cdot \vec{V}) + 2\mu \frac{\partial u}{\partial x} \\ \tau_{yy} &= \lambda(\nabla \cdot \vec{V}) + 2\mu \frac{\partial v}{\partial y} \\ \tau_{zz} &= \lambda(\nabla \cdot \vec{V}) + 2\mu \frac{\partial w}{\partial z} \\ \tau_{xy} &= \tau_{yx} = \mu \left(\frac{\partial v}{\partial x} + \frac{\partial u}{\partial y} \right) \\ \tau_{yz} &= \tau_{zy} = \mu \left(\frac{\partial w}{\partial y} + \frac{\partial v}{\partial z} \right) \\ \tau_{zx} &= \tau_{xz} = \mu \left(\frac{\partial u}{\partial z} + \frac{\partial w}{\partial x} \right) \end{aligned} \quad (5.6)$$

where \vec{V} is velocity vector, ∇ is divergence and μ denotes the molecular viscosity coefficient and λ is second viscosity coefficient. By Stoke's hypothesis:

$$\lambda = -\frac{2}{3}\mu \quad (5.7)$$

The heat flux vector β in equation 5.3 can be given as below:

$$\begin{aligned}\beta_x &= u\tau_{xx} + v\tau_{xy} + w\tau_{xz} + \kappa \frac{\partial T}{\partial x} \\ \beta_y &= u\tau_{yx} + v\tau_{yy} + w\tau_{yz} + \kappa \frac{\partial T}{\partial y} \\ \beta_z &= u\tau_{zx} + v\tau_{zy} + w\tau_{zz} + \kappa \frac{\partial T}{\partial z}\end{aligned}\tag{5.8}$$

where κ is thermal conductivity and is defined as:

$$\kappa = \frac{\gamma R}{\gamma - 1} \frac{\mu}{Pr}\tag{5.9}$$

where Pr is Prandtl number, defined as ratio of momentum diffusivity and thermal diffusivity and is set to 0.72 (for air) in this numerical study.

5.1.2 Nondimensionalization

Further, Navier-Stokes equation 5.1 is nondimensionalized based on freestream fluid properties ρ_∞ , U_∞ , T_∞ , μ_∞ and characteristic diameter of the geometry (D). The nondimensional variables can be expressed as follows:

$$\begin{aligned}\rho^* &= \frac{\rho}{\rho_\infty}, \quad u^* = \frac{u}{U_\infty}, \quad v^* = \frac{v}{U_\infty}, \quad w^* = \frac{w}{U_\infty}, \quad p^* = \frac{p}{\rho_\infty U_\infty^2} \\ x^* &= \frac{x}{D}, \quad y^* = \frac{y}{D}, \quad z^* = \frac{z}{D}, \quad t^* = \frac{t}{D/U_\infty}, \quad \mu^* = \frac{\mu}{\mu_\infty}, \quad e^* = \frac{e}{\rho_\infty U_\infty^2}\end{aligned}\tag{5.10}$$

By using above relations, Navier-Stokes equation 5.1 can be converted into nondimensional form as follows:

$$\frac{\partial \mathbf{Q}^*}{\partial t^*} + \frac{\partial \mathbf{E}^*}{\partial x^*} + \frac{\partial \mathbf{F}^*}{\partial y^*} + \frac{\partial \mathbf{G}^*}{\partial z^*} = \frac{1}{Re} \left[\frac{\partial \mathbf{E}_v^*}{\partial x^*} + \frac{\partial \mathbf{F}_v^*}{\partial y^*} + \frac{\partial \mathbf{G}_v^*}{\partial z^*} \right]\tag{5.11}$$

where Re is Reynolds number, which is defined as ratio of inertial forces and viscous forces as follows:

$$Re = \frac{\rho_\infty U_\infty D}{\mu_\infty}\tag{5.12}$$

The components of vectors $\mathbf{Q}^*, \mathbf{E}^*, \mathbf{F}^*, \mathbf{G}^*, \mathbf{E}_v^*, \mathbf{F}_v^*, \mathbf{G}_v^*$ are same as those of equation 5.1, which are replaced by nondimensional variables.

The nondimensional equation of state of perfect gas as follows:

$$p^* = \rho^* R^* T^*\tag{5.13}$$

where,

$$R^* = \frac{1}{\gamma M_\infty^2} \quad (5.14)$$

M_∞ is the free stream Mach number, which is defined as ratio of freestream velocity and freestream speed of sound:

$$M_\infty = \frac{U_\infty}{c_\infty} = \frac{U_\infty}{\sqrt{\gamma R T_\infty}} \quad (5.15)$$

The nondimensional viscous coefficient (μ^*) has been calculated by Sutherland formula:

$$\begin{aligned} \mu^* &= C_1^* \frac{(T^*)^{\frac{3}{2}}}{T^* + C_2^*} \\ C_1^* &= \frac{1.4580 \times 10^{-6}}{\mu_\infty}, \quad C_2^* = \frac{110.40}{T_\infty} \end{aligned} \quad (5.16)$$

The numerical simulations were performed in non-dimensional form of equations. Hereafter, the (*) mark has been removed for compactness.

5.1.3 Generalized Governing Equations

Further the nondimensional Navier-Stokes equation 5.11 can be transformed for generalized curvilinear coordinate system (ξ, η, ζ) where,

$$\begin{aligned} \xi &= \xi(x, y, z) \\ \eta &= \eta(x, y, z) \\ \zeta &= \zeta(x, y, z) \end{aligned} \quad (5.17)$$

By applying chain rule for partial derivatives, equation 5.11 transform as following:

$$\frac{\partial \hat{\mathbf{Q}}}{\partial t} + \frac{\partial \hat{\mathbf{E}}}{\partial \xi} + \frac{\partial \hat{\mathbf{F}}}{\partial \eta} + \frac{\partial \hat{\mathbf{G}}}{\partial \zeta} = \frac{1}{Re} \left[\frac{\partial \hat{\mathbf{E}}_{\mathbf{v}}}{\partial \xi} + \frac{\partial \hat{\mathbf{F}}_{\mathbf{v}}}{\partial \eta} + \frac{\partial \hat{\mathbf{G}}_{\mathbf{v}}}{\partial \zeta} \right] \quad (5.18)$$

$$\hat{\mathbf{Q}} = \frac{1}{J} \begin{bmatrix} \rho \\ \rho u \\ \rho v \\ \rho w \\ e \end{bmatrix}, \quad \hat{\mathbf{E}} = \frac{1}{J} \begin{bmatrix} \rho U \\ \rho u U + \xi_x p \\ \rho v U + \xi_y p \\ \rho w U + \xi_z p \\ (e + p)U \end{bmatrix}, \quad \hat{\mathbf{F}} = \frac{1}{J} \begin{bmatrix} \rho v V \\ \rho u V + \eta_x p \\ \rho v V + \eta_y p \\ \rho w V + \eta_z p \\ (e + p)V \end{bmatrix}, \quad \hat{\mathbf{G}} = \frac{1}{J} \begin{bmatrix} \rho W \\ \rho u W + \zeta_x p \\ \rho v W + \zeta_y p \\ \rho w W + \zeta_z p \\ (e + p)W \end{bmatrix} \quad (5.19)$$

$$\begin{aligned}
\hat{\mathbf{E}}_{\mathbf{v}} &= \frac{1}{J} \begin{bmatrix} 0 \\ \xi_x \tau_{xx} + \xi_y \tau_{xy} + \xi_z \tau_{xz} \\ \xi_x \tau_{yx} + \xi_y \tau_{yy} + \xi_z \tau_{yz} \\ \xi_x \tau_{zx} + \xi_y \tau_{yz} + \xi_z \tau_{zz} \\ \xi_x \beta_x + \xi_y \beta_y + \xi_z \beta_z \end{bmatrix} \\
\hat{\mathbf{F}}_{\mathbf{v}} &= \frac{1}{J} \begin{bmatrix} 0 \\ \eta_x \tau_{xx} + \eta_y \tau_{xy} + \eta_z \tau_{xz} \\ \eta_x \tau_{yx} + \eta_y \tau_{yy} + \eta_z \tau_{yz} \\ \eta_x \tau_{zx} + \eta_y \tau_{yz} + \eta_z \tau_{zz} \\ \eta_x \beta_x + \eta_y \beta_y + \eta_z \beta_z \end{bmatrix} \\
\hat{\mathbf{G}}_{\mathbf{v}} &= \frac{1}{J} \begin{bmatrix} 0 \\ \zeta_x \tau_{xx} + \zeta_y \tau_{xy} + \zeta_z \tau_{xz} \\ \zeta_x \tau_{yx} + \zeta_y \tau_{yy} + \zeta_z \tau_{yz} \\ \zeta_x \tau_{zx} + \zeta_y \tau_{yz} + \zeta_z \tau_{zz} \\ \zeta_x \beta_x + \zeta_y \beta_y + \zeta_z \beta_z \end{bmatrix}
\end{aligned} \tag{5.20}$$

U, V and W are contravariant velocities, which are defines as:

$$\begin{aligned}
U &= \xi_x u + \xi_y v + \xi_z w \\
V &= \eta_x u + \eta_y v + \eta_z w \\
W &= \zeta_x u + \zeta_y v + \zeta_z w
\end{aligned} \tag{5.21}$$

The metrics and Jacobian of transformation are given as follows:

$$\begin{aligned}
\xi_x &= J(y_\eta z_\zeta - y_\zeta z_\eta), & \xi_y &= J(z_\eta x_\zeta - z_\zeta x_\eta), & \xi_z &= J(x_\eta y_\zeta - x_\zeta y_\eta) \\
\eta_x &= J(y_\zeta z_\xi - y_\xi z_\zeta), & \eta_y &= J(z_\zeta x_\xi - z_\xi x_\zeta), & \eta_z &= J(x_\zeta y_\xi - x_\xi y_\zeta) \\
\zeta_x &= J(y_\xi z_\zeta - y_\zeta z_\xi), & \zeta_y &= J(z_\xi x_\eta - z_\eta x_\xi), & \zeta_z &= J(x_\xi y_\eta - x_\eta y_\xi)
\end{aligned} \tag{5.22}$$

$$J^{-1} = x_\xi(y_\eta z_\zeta - y_\zeta z_\eta) - x_\eta(y_\xi z_\zeta - y_\zeta z_\xi) + x_\zeta(y_\xi z_\eta - y_\eta z_\xi) \tag{5.23}$$

Here $\xi_x, \xi_y, \xi_z, \eta_x, \eta_y, \eta_z, \zeta_x, \zeta_y$ and ζ_z correspond to area vector of cell and Jacobian can be defined as ratio of volume of the cell in computational space and physical space.

5.2 Numerical Techniques

The partial differential equation 5.18 is discretized as follows:

$$\hat{Q}_{i,j,k}^{n+1} = \hat{Q}_{i,j,k}^n + \lambda R \hat{Q}_{i,j,k}^{n+1} + (1 - \lambda) R(\hat{Q}_{i,j,k}^n) \quad (5.24)$$

$$\begin{aligned} R(\hat{Q}_{i,j,k}^n) = & -\Delta t [(\hat{E}_{i+\frac{1}{2},j,k}^n - \hat{E}_{i-\frac{1}{2},j,k}^n) \\ & + (\hat{F}_{i,j,k+\frac{1}{2}}^n - \hat{F}_{i,j,k-\frac{1}{2}}^n) \\ & + (\hat{G}_{i,j,k+\frac{1}{2}}^n - \hat{G}_{i,j,k-\frac{1}{2}}^n) \\ & + (\hat{E}_{v,i+\frac{1}{2},j,k}^n - \hat{E}_{v,i-\frac{1}{2},j,k}^n) \\ & + (\hat{F}_{v,i,j+\frac{1}{2},k}^n - \hat{F}_{v,i,j-\frac{1}{2},k}^n) \\ & + (\hat{G}_{v,i,j,k+\frac{1}{2}}^n - \hat{G}_{v,i,j,k-\frac{1}{2}}^n)] \end{aligned} \quad (5.25)$$

Hence, three dimensional Navier-Stokes equation have been converted to one-dimensional flux calculations in each direction. The temporal accuracy of the scheme in equation 5.24 depends on λ , for $\lambda = 0$ it gives first order explicit scheme and $\lambda = 1$, it gives first order implicit scheme. In this study, the temporal difference of the conservative variable \hat{Q} is evaluated explicitly by setting $\lambda = 0$. The spatial inviscid fluxes \hat{E} , \hat{F} and \hat{G} are evaluated by Liou's all-speed ASUM (Advection Upstream Splitting Method)+up scheme⁵⁹ with upwind biased third order MUSCL (monotonic upstream-centered scheme for conservation laws) interpolation⁶⁰, while viscous fluxes are evaluated by central difference method.

5.2.1 Evaluation of Inviscid Fluxes

The evaluation of inviscid fluxes are done by ASUM+up scheme. However, at first Yee-symmetric TVD Scheme⁶¹ was utilized, but numerical instability along the centerline of bow shock as carbuncle instability observed for current grid configuration. Hence, ASUM+up all speed scheme is utilized here for computing inviscid fluxes. There are many schemes related to ASUM-family. The first step, which is common in all ASUM-family schemes is that the inviscid flux can be explicitly splitted into convective term and pressure term as follows:

$$E_{i+\frac{1}{2}} = \begin{bmatrix} \rho \\ \rho u \\ \rho v \\ \rho w \\ e \end{bmatrix} u_{i+\frac{1}{2}} + \begin{bmatrix} 0 \\ p_{i+\frac{1}{2}} \\ 0 \\ 0 \\ 0 \end{bmatrix} = E_{i+\frac{1}{2}}^{(c)} + \begin{bmatrix} 0 \\ p_{i+\frac{1}{2}} \\ 0 \\ 0 \\ 0 \end{bmatrix} \quad (5.26)$$

here convective term $E^{(c)}$ represent the physcial properties transported by mass flux, ρu , it can be rewritten by upwinding scheme in terms of Mach number M :

$$\begin{aligned}
 E_{i+\frac{1}{2}}^{(c)} &= u_{i+\frac{1}{2}} \begin{bmatrix} \rho \\ \rho u \\ \rho v \\ \rho w \\ e \end{bmatrix}_{i+\frac{1}{2}} = M_{i+\frac{1}{2}} \begin{bmatrix} \rho c \\ \rho cu \\ \rho cv \\ \rho cw \\ \rho ch \end{bmatrix}_{i+\frac{1}{2}} \\
 &= M_{i+\frac{1}{2}} \begin{bmatrix} \rho c \\ \rho cu \\ \rho cv \\ \rho cw \\ \rho ch \end{bmatrix}_L \quad \text{if } M_{i+\frac{1}{2}} \geq 0, \\
 &= M_{i+\frac{1}{2}} \begin{bmatrix} \rho c \\ \rho cu \\ \rho cv \\ \rho cw \\ \rho ch \end{bmatrix}_R \quad \text{if } M_{i+\frac{1}{2}} < 0,
 \end{aligned} \tag{5.27}$$

Here L and R denotes the left and right side of the cell interface. Further, Equation 5.26 - 5.27 can be written in generalized form:

$$E_{i+\frac{1}{2}} = \frac{m + |m|}{2} \Phi_L + \frac{m - |m|}{2} \Phi_R + \bar{P} \mathbf{N} \tag{5.28}$$

$$\Phi = \begin{bmatrix} 1 \\ u \\ v \\ w \\ h \end{bmatrix}, \quad \mathbf{N} = \begin{bmatrix} 0 \\ 1 \\ 0 \\ 0 \\ 0 \end{bmatrix}, \tag{5.29}$$

The difference between ASUM+up all speed scheme and general ASUM scheme is that additional pressure diffusion term M_p is introduced and for pressure flux velocity diffusion term P_u is introduced. The evaluation of pressure and mass flux is proceeded as follows:

$$\bar{P} = \beta_L P_L + \beta_R P_R + P_u \tag{5.30}$$

$$\beta_L/R = \begin{cases} \frac{1}{2}(1 \pm \text{sign}(M)) & \text{if } |M| \geq 1 \\ \frac{1}{4}(M \pm 1)^2(2 \mp M) \pm \alpha M(M^2 - 1)^2, & \text{otherwise} \end{cases} \quad (5.31)$$

Mass Flux evaluation:

$$\begin{aligned} c^{*2} &= \frac{2(\gamma - 1)}{(\gamma + 1)} h \\ \tilde{c}_L &= \frac{c^{*2}}{\max(c^*, V_n^L)} \\ \tilde{c}_R &= \frac{c^{*2}}{\max(c^*, -V_n^R)} \\ c_{\frac{1}{2}} &= \min(\tilde{c}_L, \tilde{c}_R), \\ \overline{M}^2 &= \frac{V_n^{L2} + V_n^{R2}}{2c_{\frac{1}{2}}^2}, \\ M_0^2 &= \min(1, \max(\overline{M}^2, M_\infty^2)), \\ f_a(M_0) &= M_0(2 - M_0) \\ \alpha &= \frac{3}{16}(-4 + 5f_a^2) \end{aligned} \quad (5.32)$$

$$f_M^{L/R} = \begin{cases} \frac{1}{2}(M \pm |M|) & \text{if } |M| \geq 1 \\ \pm \frac{1}{4}(M \pm 1)^2 \pm \frac{1}{2}(M^2 - 1)^2, & \text{otherwise} \end{cases} \quad (5.33)$$

$$\begin{aligned} M_{\frac{1}{2}} &= f_M^L + f_M^R + M_p \\ M_p &= 2 \frac{K_p}{f_a} \max(1 - \sigma \overline{M}^2, 0) \frac{p_R + p_L}{(\rho_L + \rho_R)c_{\frac{1}{2}}^2} \end{aligned} \quad (5.34)$$

Finally,

$$\dot{m} = M_{\frac{1}{2}} c_{\frac{1}{2}} \begin{cases} \rho_L & \text{if } M_{\frac{1}{2}} \geq 0 \\ \rho_R & \text{otherwise} \end{cases} \quad (5.35)$$

For Pressure Flux in equation 5.30, velocity diffusion term can be calculated as follows:

$$P_u = -K_u \beta_L \beta_R (\rho_L + \rho_R) f_a c_{\frac{1}{2}} (V_n^L - V_n^R) \quad (5.36)$$

where, $K_u = 0.75$, $K_p = 0.25$ and $\sigma = 1$.

The physical properties at both side of interface Q^L and Q^R are evaluated by MUSCL interpolation as follows:

$$\begin{aligned} Q_{i+\frac{1}{2}}^L &= Q_i + \left\{ \frac{s}{4} [(1 - \kappa s) \Delta_L + (1 + \kappa s) \Delta_R] \right\}_i \\ Q_{i+\frac{1}{2}}^R &= Q_{i+1} - \left\{ \frac{s}{4} [(1 - \kappa s) \Delta_R + (1 + \kappa s) \Delta_L] \right\}_{i+1} \end{aligned} \quad (5.37)$$

where,

$$s = \frac{2\Delta_L\Delta_R + \varepsilon}{(\Delta_L)^2 + (\Delta_R)^2 + \varepsilon} \quad (5.38)$$

$$\Delta_L = Q_{i+1} - Q_i, \quad \Delta_R = Q_i - Q_{i-1} \quad (5.39)$$

In this calculation $\kappa = 1/3$ has been used, which gives upwind-biased third-order scheme. $\varepsilon = 10^{-6}$ is a small number, to prevent the denominator zero for uniform region, where $\Delta_L = \Delta_R$

5.2.2 Evaluation of Viscous Fluxes

The viscous fluxes are evaluated with second-order central difference scheme. The formulation for first derivative is given as follows:

$$\frac{\partial \hat{E}_v}{\partial \xi} = \frac{\hat{E}_{v_{i+\frac{1}{2},j,k}} - \hat{E}_{v_{i-\frac{1}{2},j,k}}}{d\xi} \quad (5.40)$$

The properties at interface are evaluated as follows:

$$\begin{aligned} u_{i+\frac{1}{2}} &= \frac{u_i + u_{i+1}}{2} \\ v_{i+\frac{1}{2}} &= \frac{v_i + v_{i+1}}{2} \\ w_{i+\frac{1}{2}} &= \frac{w_i + w_{i+1}}{2} \\ \mu_{i+\frac{1}{2}} &= \frac{\mu_i + \mu_{i+1}}{2} \end{aligned} \quad (5.41)$$

Further the first derivatives are evaluated as:

$$\begin{aligned} \frac{\partial f}{\partial x} &= \frac{\partial f}{\partial \xi} \frac{\partial \xi}{\partial x} + \frac{\partial f}{\partial \eta} \frac{\partial \eta}{\partial x} + \frac{\partial f}{\partial \zeta} \frac{\partial \zeta}{\partial x} \\ \frac{\partial f}{\partial y} &= \frac{\partial f}{\partial \xi} \frac{\partial \xi}{\partial y} + \frac{\partial f}{\partial \eta} \frac{\partial \eta}{\partial y} + \frac{\partial f}{\partial \zeta} \frac{\partial \zeta}{\partial y} \\ \frac{\partial f}{\partial z} &= \frac{\partial f}{\partial \xi} \frac{\partial \xi}{\partial z} + \frac{\partial f}{\partial \eta} \frac{\partial \eta}{\partial z} + \frac{\partial f}{\partial \zeta} \frac{\partial \zeta}{\partial z} \end{aligned} \quad (5.42)$$

Here function's derivatives with respect to ξ , η and ζ are evaluated as follows:

$$\begin{aligned}\left.\frac{\partial f}{\partial \xi}\right|_{i+\frac{1}{2}} &= (f_{i+1,j,k} - f_{i,j,k}) \\ \left.\frac{\partial f}{\partial \eta}\right|_{i+\frac{1}{2}} &= \frac{1}{4}[f_{i,j+1,k} - f_{i,j-1,k} + f_{i+1,j+1,k} - f_{i-1,j-1,k}] \\ \left.\frac{\partial f}{\partial \zeta}\right|_{i+\frac{1}{2}} &= \frac{1}{4}[f_{i,j,k+1} - f_{i,j,k-1} + f_{i+1,j,k+1} - f_{i-1,j,k-1}]\end{aligned}\quad (5.43)$$

All the derivatives in other directions are computed in the same manner.

5.2.3 Time Integration

To have better time accuracy in unsteady flow simulation, third-order three step TVD Runge-Kutta method⁶² is used for time integration, which can be described below:

$$\begin{aligned}\hat{Q}^{(1)} &= \hat{Q}^n + \Delta t f(\hat{Q}^n) \\ \hat{Q}^{(2)} &= \frac{3}{4}\hat{Q}^n + \frac{1}{4}\hat{Q}^{(1)} + \frac{1}{4}\Delta t f(\hat{Q}^{(1)}) \\ \hat{Q}^{n+1} &= \frac{1}{3}\hat{Q}^n + \frac{2}{3}\hat{Q}^{(2)} + \frac{2}{3}\Delta t f(\hat{Q}^{(2)})\end{aligned}\quad (5.44)$$

5.3 Problem Setting

The unsteady compressible laminar Navier-Stokes equations have been solved for three basic geometries as convex blunt nose, flat plate and concave hemispherical shell at hypersonic Mach number 7. In this section, description of computational domain have been given for these three geometries, further boundary conditions and initial conditions are described. And, data extraction method has been mentioned.

5.3.1 Computational Domain

In a first step, a curvilinear two dimensional grid is generated by elliptic grid generation method⁶³ and further rotated around the centerline axis to generate three dimensional grid system. Figure 5.1a and 5.1b shows the two dimensional elliptic grid for flat plate and convex geometries, respectively and zoomed view for a section of three dimensional grid. The grid for flat plate and convex geometries consists of $151 \times 151 \times 151$ points. The grid domains shown in the figures are already non-dimensionalized with the reference diameter of geometry as 30 mm. The nondimensionalized minimum grid spacing for flat and convex geometries are 2.1×10^{-4} . In case of flat plate and convex geometry, the domain extent along the x-direction is $-1 \leq x/D \leq 15$, while in y- and z-direction maximum extent is

Note:

Further contents of Chapter 5 are planned to be part of published Journal articles in future.

The pages 127 - 130 in Chapter 5 will be open to public after September 16, 2021.

Chapter 6

Numerical Results

The experimental analysis of bow shock instability was performed by force measurement and flow visualization by using Schlieren system. However, the Schlieren system can provide the limited flow field information in two-dimensional image plane. To further understand the three dimensionality of physical phenomenon, unsteady Navier-Stokes equations have been solved for flat, convex and concave shape blunt nose. In this chapter, numerical results have been analyzed for the same three basic geometries. However, the computation for flat and convex geometry is stable and flow field is simulated for 2 ms., but for concave shape geometry the numerical simulation breaks down when there is onset of large deformation of bow shock in front of concave shape geometry before 2 ms. In this chapter, initially, the numerical results are analyzed for flat and convex geometries and drag coefficient and shock feature are compared with the experiments. Further, the numerical results for three grid configurations for concave shape have been compared with experiments for time averaged drag coefficients and shock stand off distances during linear damped motion of bow shock. The dynamics of large deformation patterns from numerical simulations for these three grid configurations have been analyzed before simulation stops.

6.1 Numerical Results for Flat and Convex Geometry

The computation for flat plate geometry and convex shape geometry was performed for $151 \times 151 \times 151$ grid size for each as discussed in Chapter 5. The main purpose of doing the numerical analysis for flat and convex geometries is to validate the numerical simulation code with experimental measurement for less unsteady flow field geometries and the other purpose is to understand the flow phenomenon in case of bigger stagnation zone of flat plate. The numerical analysis is done by comparing drag force and shock stand off distance after 2 ms of computation and by analyzing non-dimensional pressure

Note:

Further contents of Chapter 6 are planned to be part of published Journal articles in future.

The pages 132 - 145 in Chapter 6 will be open to public after September 16, 2021.

Chapter 7

Discussion on Bow shock Instability Mechanism

In this chapter, discussion have been made for bow shock instability mechanism from the understanding obtained from experimental study of basic geometries, the effect of various control methods and numerical analysis for concave shape geometry.

7.1 Findings from Experimental and Numerical Studies

It is clear from force measurement study for basic geometries, that the concave shape have a higher drag coefficient than a convex shape blunt nose of same reference area, while, it has slightly lesser drag coefficient than the flat plate. From the flow visualization experiments, it is found that the bow shock exhibits violent fluctuations in front of concave shape geometry in comparison to flat and convex shape geometry. The shock displacement analysis, give information that the bow shock in front of concave shape geometry behaves as nonlinear duffing oscillator system. From, the double peak probability density function, a double well potential function can be plotted, which provides information that the bow shock fluctuations have two stable states, one with lower potential and other one with higher potential and almost neutral stable from one side. It means that the bow shock returns to its lower potential state, after losing its all energy during large bow shock fluctuations. The high pressure gradient in the thin shock layer for convex and flat plate can be understood as a linear restoring force for these geometries and, viscous dissipation can work as damping. Hence, bow shock in front of convex or flat plate system can be assumed as linear harmonic oscillator. Any freestream disturbances or vorticity generated by bow shock can be highly damped in very short time.

The cavity in front of concave shaped blunt nose offers larger volume for vorticity generated by

Note:

Further contents of Chapter 7 are planned to be part of published Journal articles in future.

The pages 147 - 158 in Chapter 7 will be open to public after September 16, 2021.

Chapter 8

Conclusions

The main objective of this study is to understand the flow phenomenon involved in large amplitude bow shock fluctuations in front of concave shaped blunt nose and further to study the effectiveness of passive flow control methods to provide the effective flow control for bow shock fluctuations as well as to strengthen the understanding of bow shock fluctuations by understanding the effect of different passive control methods on the bow shock fluctuations. The secondary objective was to establish the analysis methods for highly unsteady flow field around the concave shaped blunt nose. These objective have been achieved as follows:

- In force measurement experiments, it is found that the concave hemispherical shell has drag coefficient 1.598, which is very close to flat circular plate (1.771) and it is approximately 1.7 times than convex shape blunt nose (0.921). The unsteady flow field around the concave shape blunt nose have been characterized by lift and side force coefficient plot, which was later used while comparing the effects of control mechanism.
- The image processing method was established to compute the bow shock displacements by using time-resolved Schlieren system with high-speed camera.
- The bow shock displacement analysis by probability density function provides two dominating peaks, which gives information that the bow shock in front of concave shaped blunt nose system behaves as a nonlinear duffing oscillator, which has two energy states, one stable, while the other one similar to neutral stable.
- It is conceptualized that high pressure behind the bow shock may work as restoring force, the ease of flow to pass from the body surface (viscous dissipation) may work as damping. The

region between the bow shock and the concave body have larger volume than in compare to flat and convex geometry. The vorticity introduced by bow shock stay in the cavity and may be the reason for restoring force to behave like nonlinear restoring force as in case of duffing oscillator.

- From bow shock instability patterns, it is found that flow disturbance in form of particle or vortical disturbances are mainly responsible for onset of large amplitude bow shock fluctuations in case of concave shaped blunt nose. However, in case of flat and convex case, these flow disturbances also disturb the bow shock, but bow shock retains its position again with in 0.1 ms and 0.6 ms for convex and flat plate, respectively. In case of concave shape, large deformations in bow shock may last from 10 ms to 300 ms.
- The proper orthogonal decomposition for the time resolved Schlieren image data was performed for large amplitude bow shock deformation in front of concave shaped blunt nose. The first two modes are found to be associated with back and forth flow motion and side-ward flow motion, respectively. with relative energy of 25 % and 12 %, respectively The higher modes are either harmonics of these modes or mixed modes.
- The change in angle of attack in front of concave shape geometry leads to increase in bow shock stability with increase in angle of attack. The critical angle of attack is found as 7° , above which bow shock remain almost stable.
- Among the passive control methods studied, crosswire control works best with performance index as 74.88 %, then the spike control with 66.26 %. The performance of flat base, notch and tab controls found to be similar approximately 15 ~ 21%. Breathing control performs worst. The performance index tells the probability of bow shock always remain close to the body.
- On the basis of study of each flow control, it was confirmed that the bow shock instabilities in front of concave shaped blunt nose is because of some growth of vortex in the cavity, which was the reason for nonlinearity of the system and crosswire works effectively to manipulate the large vortex inside the cavity to remove nonlinearity of the system.
- Numerical simulations provide three-dimensional information of flow behavior inside the cavity during the onset of large deformation of bow shock.
- Based on experimental studies of basic geometry and control methods and numerical study of concave shape geometry, the mechanism of bow shock instability is explained as interaction of vorticities generated by bow shock along with flow disturbances, leads to deformation in vortex ring in the cavity. The deformed vortex ring make large circulation in the cavity, which leads to large deformation of bow shock.
- Further, effectiveness of control methods is explained by the bow shock instability mechanism.

References

1. Rathakrishnan E. (2010) "Fluid Mechanics: An Introduction," Third Edition, Prentice Hall India, New Delhi, India.
2. Rathakrishnan E. (2010) "Applied Gas Dynamics," First Edition, John Wiley (Asia) Pvt. Ltd, Singapore.
3. Rathakrishnan E. (2007) "Instrumentation, Measurements, and Experiments in Fluids," CRC Press, Taylor and Francis, USA.
4. Anderson J.D. Jr. (2006) "Hypersonic and High Temperature Gas Dynamics," Second Edition, AIAA Education Series, USA.
5. Bertin J. J. (1994) "Hypersonic Aerothermodynamics," AIAA Education Series, USA.
6. Fujii K., Tsuda S., Koyama T., and Hirabayshi N. (2013) "Oscillation of Bow Shock Waves at Hypersonic Speeds," AIAA Paper 2013-3103.
7. Hopko R.H., Strass H.K. (March 1958) "Some Experimental Heating Data on Convex and Concave Hemispherical Nose Shapes and Hemispherical Depressions on a 30° Blunted Nose Cone," NACA RM L58A17a.
8. Cooper M., Beckwith I.E., Jones J.J., Gallagher J.J. (July 1958) "Heat Transfer Measurements on a Concave Hemispherical Nose Shape with Unsteady Flow Effects at Mach Numbers of 1.98 and 4.95," NACA RM L58D25a.
9. Markley T.J. (July 1958) "Heat Transfer and Pressure Measurement on a 5-inch Hemispherical Concave Nose at Mach Numbers of 2.0," NACA RM L58C14a.
10. Levine J., Rumsey C.B. (December 1958) "Heat Transfer Measurements on a 5.5-inch Hemispherical Concave Nose in free flight at Mach Numbers up to 6.6," NASA MEMO 10-21-58L.
11. Johnson R.H. (1959) "Instability of Hypersonic Flow About Blunt Bodies," Physics of Fluids, Vol.2, No.5, pp. 526-532.

12. Baryshnikov A.S., Bedin A.P., Maslennikov V.G., Mishin G.I. (1979) "Stability of Bow Shock," Soviet Technical Physics Letters, 5, pp. 113-114.
13. Bastianon R.A. (1969) "Unsteady Solution of the Flowfield over Concave Bodies," AIAA Journal, Vol. 7, No.3, pp.531-533.
14. Bohachevsky I.O., Kostoff R.N. (1972) "Supersonic flow over Convex and Concave Shapes with Radiation and Ablation Effect," AIAA Journal, Vol. 10, No. 8, pp.1024-1031.
15. Sambamurthi J.K., Huebner L.D., Utreja L.R. (1987) "Hypersonic Flow Over a Cone with Nose Cavity," AIAA Paper 87-1193.
16. Hartmann J., Troll B. (1922) "On a new method for the generation of sound waves," Phys Rev. 20, 719.
17. Huebner L.D., Utreja L.R. (1993) "Mach 10 Bow-Shock Behavior of a Forward-Facing Cavity," Journal of Spacecraft and Rockets, Vol. 30, No.3, pp.291-297.
18. Yuceil B., Dolling D.S. (1994) "Effect of nose cavity on heat transfer and flow field over blunt body at Mach 5," AIAA Paper 1994-2050.
19. Engblom W.A., Yuceil B., Goldstein D.B. and Dolling D.S. (1996) "Experimental and Numerical Study of Hypersonic Forward-Facing Cavity Flow," AIAA Paper 1994-2050.
20. Engblom W.A., Goldstein D.B., Ladoon D., Schneider S.P. (1997) "Fluid Dynamics of Forward Facing Cavity," Journal of Spacecraft and Rockets, Vol.34, N0.4, pp. 437-444.
21. Ladoon D.W., Schneider S.P., Schmisser J.D. (1998) "Physics of Resonance of Forward -Facing Cavity," Journal of Spacecraft and Rockets, Vol.35, N0.5, pp. 626-632.
22. Juliano T.J., Segura R., Borg M.P., Casper K., Hanon M.J. Jr., Wheaton B.M. Schneider S.P. (2008), "Starting Issue and Forward-Facing Cavity Resonance in Hypersonic Quiet Tunnel," AIAA-Paper 2008-3735
23. Engblom W., Goldstein D (2009), "Acoustic Analogy for Oscillations Induced by Supersonic Flow over a Forward-Facing Nose Cavity," AIAA-Paper 2009-384
24. Yadav R., Guven U. (2014), "Aerothermodynamics of a hypersonic vehicle with a forward facing parabolic cavity at nose," Proceedings of IMECH-E, Journal of Aerospace Engineering, Vol. 228, No.10, pp. 1863-1874.
25. Yadav R., Guven U. (2015), "Aerodynamic Heating of a Hypersonic Projectile with Forward-Facing Ellipsoidal Cavity at Nose," Journal of Spacecrafts and Rockets, Vol. 52, No.1, pp. 157-165.

26. Hiraki K., Hinada M., Nakajima T., Inatani Y. (1992), "The Aerodynamic Characteristics of Cup-like Body in Supersonic Flow," Proceedings of 18th International Symposium of Space Technology and Science, pp.741
27. Hiraki K., Kleine H. (2004), "Dynamic behavior of the shock wave formed around a reflector in supersonic flow," Proceedings of the 24th International Symposium on Shock Waves Beijing, China pp.167-172.
28. Mizukaki T., Kawamura N. (2012), "Instability Characteristics of Shock Waves ahead of a Hemispherical Shell at Supersonic Speeds," 28th Congress of the International Council of the Aeronautical Science, ICAS 2012-11.4.2.
29. Ohnishi N., Sato Y., Kikuchi Y., Ohtani K., Yasue K. (2015), "Bow-Shock Instability induced by Helmholtz resonator like feedback slipstream," Physics of Fluids Vol.27, 066103.
30. Hatanaka K., Rao S.M.V., Saito T., Mizukaki T.. (2016), "Numerical Investigation on Shock oscillations ahead of hemispherical shell in Supersonic Flow," Shock Waves, Vol. 27, DOI: 10.1007/s00193-015-0613-0 .
31. Zhuang N., Alvi F., Alkislar M. (2006), "Supersonic cavity flows and their Control," AIAA Journal Vol.44, No.9, pp.2118-2128.
32. Venukumar B., Jagadeesh G., Reddy K.P.J (2006), "Counterflow drag reduction by supersonic jet for a blunt body in hypersonic flow," Physics of Fluids, Vol. 18, 118104.
33. Raman G., Khanafseh S., Cain A.B., Kerschen E. (2004), "Development of high bandwidth powered resonance tube actuators with feedback control," Journal of Sound and Vibration, Vol.269, No.3-5, pp.1031-1062.
34. Crittenden T., Glezer A., Funk R., Parekh D. (2001), "Combustion-driven jet actuators for flow control," AIAA Paper 2001-2768.
35. Satheesh K., Jagadeesh G. (2007), "Effect of concentrated energy deposition on the aerodynamic drag of a blunt body in hypersonic flow," Physics of Fluids, Vol. 19, 031701.
36. Watanabe Y., Suzuki K. (2011), "Effect of Impulsive Plasma Discharge in Hypersonic Boundary Layer over a Flat Plate," AIAA Paper 2011-3736.
37. Khurana S., Suzuki K. (2013), "Application of Aerospike for Lifting Body Configuration in Hypersonic Flow at Mach 7," AIAA Paper 2013-3113.
38. Imamura O., Watanuki T., Suzuki K., Rathakrishnan E., "Breathing Blunt Nose for drag reduction at Hypersonic Speeds," Journal of Visualization, Vol.11, No.4., pp.280-280.

39. Watanabe Y., Suzuki K., Rathakrishnan E. (2016), "Aerodynamic Characteristics of breathing blunt nose configuration at hypersonic speeds," Proceedings of the Institute of Mechanical Engineers, Part G: Journal of Aerospace Engineering, doi: 10.1177/0954410016643979.
40. Vashishtha A., Rathakrishnan E. (2009), "Breathing Blunt Nose Concept for drag reduction in Supersonic Flow," Proceedings of the Institute of Mechanical Engineers, Part G: Journal of Aerospace Engineering, Vol. 223, No.1, pp. 31-38.
41. Wernet M.P., Locke R.J., Wroblewski A., Sengupta A. (2009), "Application of Stereo PIV on Supersonic Parachute Model," AIAA Paper 2009-0070.
42. Clement S., Rathakrishnan E. (2006), "Characteristics of Sonic Jets with Tabs," Shock Waves, Vol. 15, No. 3, pp. 219-227.
43. Verma S.B., Rathakrishnan E. (2002), "Noise field of underexpanded Notched Circular Slot Jets," Noise and Vibration, Vol. 33, No.6, pp.9-23.
44. Rathakrishnan E. (2009), "Experimental Studies on the Limiting Tabs," AIAA Journal Vol. 47, No. 10, pp. 2475-2485.
45. Lobb R.K. (1964), "Experimental measurement of shock detachment distance in spheres fired at in air at hypervelocities," In The High Temperature Aspects of Hypersonic Flow (ed. W.C. Nelson), Pergamon, pp. 519-527.
46. Imamura O., Watanuki T., Suzuki K., Kashiwa Wind Tunnel Working Group (2007), "Flow Characteristics of UT-Kashiwa hypersonic wind tunnel," JAXA Special Publication, JAXA-SP-07-016, pp.50-55 (in Japanese).
47. Vashishtha A., Watanabe Y., Suzuki K. (2015), "Study of Shock Shape in front of Concave, Convex and Flat Arc in Hypersonic Flow," JAXA Special Publication, JAXA-SP-14-010, pp.127-132.
48. Vashishtha A., Watanabe Y., Suzuki K. (2015), "Study of Bow-Shock Instabilities in front of Hemispherical Shell at Hypersonic Mach Number 7," AIAA Paper 2015-2638.
49. Bradski G. (2000), "The opencv library," Doctor Dobbs Journal of Software Tools, Vol. 25, No.11, pp. 120-126.
50. Estruch D., Lawson N.J., Macmanus D.G., Garry K.P. Stollery J.L. (2008), "Measurement of shock wave unsteadiness using a high speed Schlieren system and digital image processing," Review of Scientific Instruments, Vol. 79, 126108.

51. Kovasznay L.S.G. (1953), "Turbulence in Supersonic Flow," Journal of Aerospace Sciences, Vol. 20, No. 10, pp. 657-674,682.
52. Kulite Products details XCL-152, <http://www.kulite.com/docs/products/XCL-152.pdf>, accessed on May 31, 2016.
53. Rong H., Wang X., Meng G., Xu W., Fang T. (2006), "On Double Peak Probability Density Functions of a Duffing Oscillator To combined deterministic and Random Exitation," Applied Mathematics and Mechanics, Vol.27, No.11, pp.1569-1576.
54. Chabreyrie R., Aubry N. (2011), "Switching chaos on / off in Duffing Oscillator" Nonlinear Sciences, Chaotic Dynamics, arXiv:1108.4118v1[nlin.CD]
55. Rault A., Chiavassa G, Donat R. (2003), "Strong-Vortex Interaction at High Mach Numbers" Journal of Scientific Computing, Vol. 19, No.1-3, pp. 347-371.
56. Lehoucq R.B., Sorensen D.C, Yang C. (1998), "ARPACK User's Guide: Solution of Large Scale Eigenvalue Problems with Implicit Restart Arnoldi Methods" Society of Industrial Applied Mathematics (SIAM).
57. Sharma H, Vashishtha A., Rathakrishnan E. (2008), "Twin-vortex flow physics," Proceedings of the Institute of Mechanical Engineers, Part G: Journal of Aerospace Engineering, Vol. 222, No.6, pp. 783-788.
58. Anderson J.D. Jr. (1995), "Computations Fluid Dynamics: The basics with application," International Edition, McGraw-Hill Inc, Singapore.
59. Liou M.S. (2006), "A sequel to ASUM, Part II: $ASUM^+$ -up for all speeds," Journal of Computational Physics, Vol.214, No.1, pp 137-170
60. Hirsch C. (2007), "Numerical Computation of Internal and External Flows Vol.1: Fundamental of Computational Fluid Dynamics," 2nd Edition, John Wiley and Sons, Singapore.
61. Yee H.C. (1989), "A class of High-Resolution Explicit and Implicit Shock Capturing Methods," NASA-TM 101088.
62. Shu C.W., Osher S. (1988), "Efficient implimentation of essentially non-oscillatory shock capturing schemes," Journal of Computational Physics, Vol.77, No.2, pp 439-471.
63. Steger J.L., Sorenson R.L. (1979), "Automatic Mesh-Point Clustering Near a Boundary in Grid Generation with Elliptic Partial Differential Equations ," Journal of Computational Physics, Vol.33, No.3, pp 405-410.

-
64. Hossain M.S., Bergstorm D.J., Chen X.B. (2015), "Visualization and analysis of large-scale vortex structures in three-dimensional turbulent lid-driven cavity flow", *Journal of Turbulence*, Vol. 16, No. 10, pp. 901-924.

Appendices

Appendix A

Proper Orthogonal Decomposition : Method of Snapshots

The method of snapshots is a discretization method to obtain proper orthogonal decomposition modes in temporal domain. In this study, it is performed on the Schlieren images, which were converted into image data vectors (of size M) to form image time matrix ($M \times N$). Lets assume there are n number of such image data vectors, given for n number of time steps, then

$$I_N(x, y) = I(x, y, t_N), \quad \text{with } N = 1, 2, 3, \dots, n \quad (\text{A.1})$$

The base image can be defined as an time averaged image of N number of snapshots:

$$I_0(x, y) = \frac{1}{N} \sum_{n=1}^N I_N(x, y) \quad (\text{A.2})$$

Each snapshot can be decomposed into the time averaged value and instantaneous fluctuations as

$$I(x, y, t_N) = I_0(x, y) + I'(x, y, t_N) \quad (\text{A.3})$$

These fluctuation vectors can form the image fluctuation - time matrix A, and the correlation matrix C can be calculated as

$$C = A^T A \quad (\text{A.4})$$

The correlation matrix will be square symmetric matrix. The proper orthogonal decomposition

requires solution of eigenvalue problem

$$CV = \lambda V \quad (\text{A.5})$$

where V is the matrix of eigenvectors of C and λ_i are its eigenvalues. If the eigenvectors are normalized, they can form the orthonormal basis and mode shapes can be constructed as follows:

$$\phi_i(x, y) = \frac{1}{\sqrt{\lambda_i N}} \sum_{n=1}^N I'(x, y, t_N) v_{N,i} \quad (\text{A.6})$$

where $v_{N,i}$ is the N^{th} element of i^{th} eigenvector of C .

In this study, ARPACK library⁵⁶ have been utilized to compute the first few eigenvalues and eigenvectors of matrix C . ARPACK library has advantage that it is not required to calculate the large matrix C , only the image fluctuation vectors can be given as input for the desired number of snapshots.

List of Publications

COMMUNICATED PAPERS

- A. Vashishtha, Y. Watanabe, K. Suzuki (2015), “Study of Shock Shape in front of Concave. Convex and Flat Arc in Hypersonic flow”, JAXA Special Publication: Proceedings of 46th Fluid Dynamics Conference / 32nd Aerospace Numerical Simulation Symposium, JAXA-SP-14-010, pp. 127-132.
- A. Vashishtha, Y. Watanabe, K. Suzuki (2015), “Study of Bow-Shock instabilities in front of Hemispherical Shell at Hypersonic Mach Number 7,” 45th AIAA Fluid Dynamics Conference, AIAA Paper 2015-2638.
- A. Vashishtha, Y. Watanabe, K. Suzuki (2016), “Bow-Shock instabilities and its Control in front of Hemispherical Concave Shell at Hypersonic Mach Number 7,” Transaction of JSASS, Aerospace Technology Japan (accepted for publication).